

## The amblygonite (LiAlPO<sub>4</sub>F)-montebrasite (LiAlPO<sub>4</sub>OH) solid solution: A combined powder and single-crystal neutron diffraction and solid-state <sup>6</sup>Li MAS, CP MAS, and REDOR NMR study

LEE A. GROAT,<sup>1,\*</sup> BRYAN C. CHAKOUMAKOS,<sup>2</sup> DARREN H. BROUWER,<sup>3</sup> CHRISTINA M. HOFFMAN,<sup>4</sup>  
COLIN A. FYFE,<sup>3</sup> HEIKO MORELL,<sup>3</sup> AND ARTHUR J. SCHULTZ<sup>5</sup>

<sup>1</sup>University of British Columbia, Department of Earth and Ocean Sciences, 6339 Stores Road, Vancouver, British Columbia V6T 1Z4, Canada

<sup>2</sup>Solid State Division, Oak Ridge National Laboratory, Oak Ridge, Tennessee 37831-6393, U.S.A.

<sup>3</sup>University of British Columbia, Department of Chemistry, 2036 Main Mall, Vancouver, British Columbia V6T 1Z1, Canada

<sup>4</sup>Spallation Neutron Source, Building 360, Argonne National Laboratory, Argonne, Illinois 60439-4814, U.S.A.

<sup>5</sup>Intense Pulsed Neutron Source, Building 360, Argonne National Laboratory, Argonne, Illinois 60439-4814, U.S.A.

### ABSTRACT

The amblygonite-montebrasite series of minerals, common constituents of granitic pegmatites and topaz-bearing granites, show complete solid solution with ideal composition LiAlPO<sub>4</sub>(F, OH). These compounds are ideal for studying F ↔ OH solid solution in minerals because natural members of the series generally show little deviation from the ideal composition. In this study, we used powder and single-crystal neutron diffraction and solid-state <sup>6</sup>Li MAS, CP MAS, and REDOR NMR techniques to study the effect of F ↔ OH substitution on the series.

Lattice parameters refined from single-crystal neutron diffraction data show increasing *b* and decreasing *a*, *c*, and *V* with increasing F/(F + OH). The volume is highest for the OH end-member because of the presence of an additional atom (H). The *a* and *c* parameters decrease with increasing F/(F + OH) because the O-H vector is close to the **a-c** plane and the Al-OH/F vectors are approximately parallel to **c**. Lattice parameters refined from neutron powder diffraction patterns collected at lower *T* show that thermal contraction increases with F/(F + OH), presumably because the F anion takes up less space than the OH molecule.

The results show that the OH/F position is always fully occupied. The H displacement ellipsoid shows little change with occupancy, which obviously corresponds negatively with increasing F/(F + OH). However, the Li displacement ellipsoid becomes extremely large and anisotropic with increasing F fraction. Most of the distortion is associated with the *U*<sub>3</sub> eigenvalue, which lies between the **c** and **c\*** directions. *U*<sub>eq</sub> values corresponding to the Li atom show a greater reduction with decreasing temperature than the other atoms. The temperature dependence of Li is the same regardless of F content. Even when extrapolated to absolute zero the Li displacement ellipsoid is very large, which implies a large static disorder.

At the montebrasite end of the series, there are five short Li-φ (φ = O, OH, F) distances and one very long Li-O4 bond. With increasing F content, the Li-O4 distance decreases and the Li-O3f distance increases, such that at the amblygonite end, the coordination is 4 + 2. The disorder in the Li site is obviously caused by the substitution of F for OH. The driving force is the loss of the hydrogen bond to O4, which causes the Li-O4 bond to strengthen and improves the bond valence to O4. The results show that the H atom position is imbedded *within* the distorted octahedral oxygen coordination of the Li atom.

To represent the disorder better, we used a split Li site model. The results show that Li1 occupancy increases and the Li2 occupancy decreases with increasing F content, and that the Li1-Li2 distance is longer for intermediate compositions than for the end-members.

The <sup>6</sup>Li MAS NMR experiments provide important structural information complementary to the neutron diffraction results. The spectra of samples in the amblygonite-montebrasite series show two well-resolved peaks, confirming the presence of Li disorder over two distinct sites, and highly resolved <sup>6</sup>Li MAS NMR spectra are obtained at the very high magnetic field strength of 18.8 T. The peaks at -0.3 ppm and -0.9 ppm were unambiguously assigned to the Li2(OH) and Li1(F) sites found in the neutron diffraction structures. The isotropic chemical shifts are consistent with the coordinations of these Li sites found in the neutron diffraction structures. The relative intensities of the two peaks across the series of samples reflect the varying F/(F + OH). In addition to confirming the assignments of the peaks, it is possible to measure H-Li2 and F-Li1 internuclear distances by

\* E-mail: lgroat@eos.ubc.ca

$^6\text{Li}\{^1\text{H}\}$  and  $^6\text{Li}\{^{19}\text{F}\}$  CP and REDOR NMR that are consistent with the corresponding distances from the neutron diffraction structures. The  $^6\text{Li}\{^1\text{H}\}$  and  $^6\text{Li}\{^{19}\text{F}\}$  CP and REDOR results indicate that the Li disorder is random throughout the crystals rather than over large domains, a conclusion that cannot be made from diffraction experiments. Variable temperature  $^6\text{Li}$  MAS NMR spectra confirm that the disorder is static and there is no dynamic exchange involving F, OH, or Li. Each Li ion has access to only one of the two observed sites as determined by the presence of either OH or F in its immediate environment and there is no possibility of a dynamic exchange.

## INTRODUCTION

The ambygonite-montebbrasite series shows complete solid solution with ideal composition  $\text{LiAlPO}_4(\text{F}, \text{OH})$ . They are common constituents of F- and Li-rich granitic pegmatites, where individual crystals may be several meters in size, and they are also found in F-rich topaz-bearing granites. The ambygonite-montebbrasite solid solution has been examined by many workers, particularly with regard to the development of a rapid physical method for the determination of the  $\text{F}/(\text{F} + \text{OH})$  ratio or the F content (Moss et al. 1969; Dubois et al. 1972; Černá et al. 1973; Fransolet and Tarte 1977; Kallio 1978; Greiner and Bloss 1987). Hydroxyl  $\leftrightarrow$  fluoride solid solutions are important in several oxysalt families, including amphiboles, apatite, epidote, crandallite, humite, micas, pyrochlore, and topaz. The ambygonite minerals are ideal for studying  $\text{F} \leftrightarrow \text{OH}$  solid solution in minerals because natural members of the series generally show little deviation from the ideal composition, so that the effects of other cation substitutions are negligible. Although tavorite ( $\text{LiFe}^{3+}\text{PO}_4\text{F}$ ) is isostructural with ambygonite, it only occurs as an alteration product of primary phosphates in pegmatites; consequently,  $\text{Al} \leftrightarrow \text{Fe}$  substitution in ambygonite-montebbrasite is rare to nonexistent (Černá et al. 1973; Groat et al. 1990).

The structures of ambygonite and montebbrasite were solved by Simonov and Belov (1958) and Baur (1959a, 1959b). The crystal structure is triclinic with space group  $P\bar{1}$  and consists of a corner-linked mixed tetrahedral-octahedral framework (Fig. 1). Corner-sharing aluminate octahedral chains extend along  $c$ , and these are cross-linked by phosphate tetrahedra (Fig. 1). This polyhedral framework topology is common to many minerals, including arsenates (durangite, tilasite), germanates, phosphates (isokite, lacroixite, natromontebbrasite, panasqueiraite, tavorite), selenates, silicates (malayaite, titanite), and sulfates (dwornikite, gunningite, kieserite, poitevinite, szmikite, and szmolnokite). All crystallize in space group  $C2/c$  except natromontebbrasite (triclinic), tilasite ( $Cc$ ), relatively pure titanite ( $P2_1/c$ ), and ambygonite-montebbrasite ( $P\bar{1}$ ). Adequate explanations for these symmetry differences have not yet been proposed (Hawthorne et al. 1987). The framework topology is also seen in synthetic materials such as  $\text{KTiPO}_4\text{O}$  (KTP), which is widely used in the optical industry for frequency doubling (Satyanarayan et al. 1999).

The bridging anion in the octahedral chains is OH or F. There are one P site, two Al sites (both at special positions), one six-fold-coordinated Li site, one H site, and five anion positions in the structure of the ambygonite-montebbrasite minerals. Simonov and Belov (1958) reported a large and extremely anisotropic displacement parameter for the Li atom and sug-

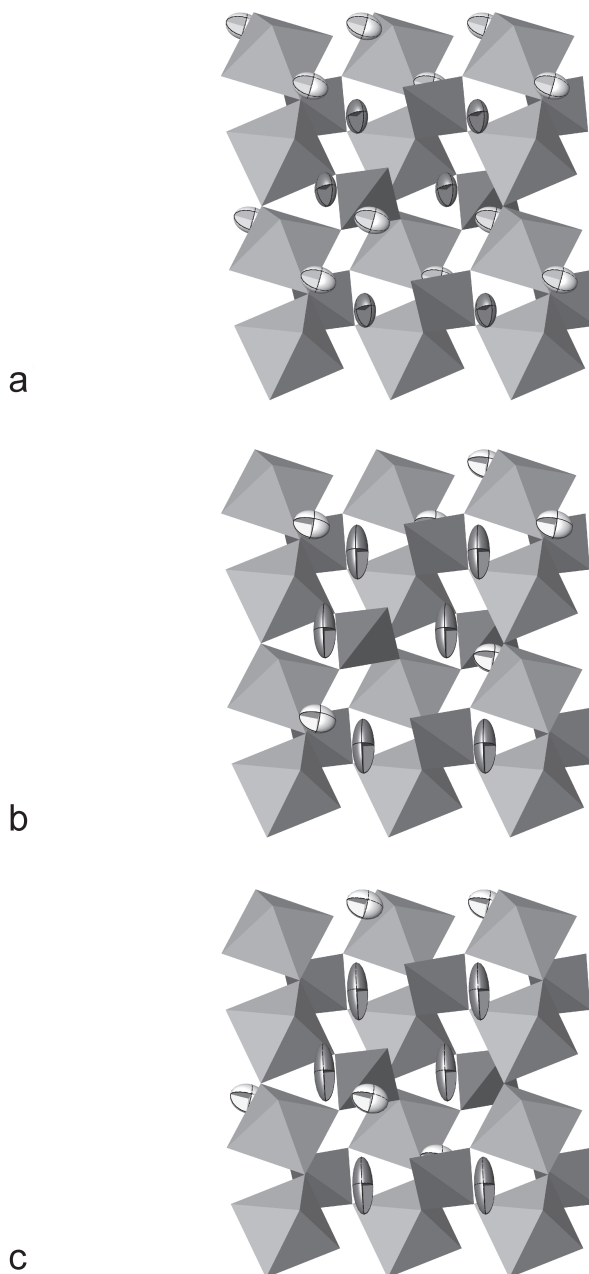


**FIGURE 1.** The crystal structures of the ambygonite-montebbrasite samples used in this study projected parallel to  $[100]$  ( $c$  vertical). (a) Dunton mine sample,  $\text{F}/(\text{F} + \text{OH}) = 0.04$ ; (b) Tanco mine sample,  $\text{F}/(\text{F} + \text{OH}) = 0.45$ ; (c) AF-46,  $\text{F}/(\text{F} + \text{OH}) = 0.55$ .

gested that the site is split into two fractionally occupied positions. Baur (1959a, 1959b) found no such splitting in the structure of montebrasite. In a subsequent single-crystal X-ray diffraction (XRD) study of the series, Groat et al. (1990) refined Li in two sites, with occupancies fixed (at 50% each) and the isotropic displacement factors constrained to be equal. They found that the Li1-Li2 distance varies nonlinearly from 0.2 to approximately 0.5 Å with increasing F/(F + OH) content.

The present study is a continuation of the single-crystal XRD study of Groat et al. (1990) and was prompted by the availability of a single-crystal neutron diffractometer and improved MAS-NMR instrumentation. The main advantage of neutron diffraction is that the scattering factors of H and Li are much greater for neutrons than for X-rays, more on par with those of P, Al, and O. Indeed, for neutron diffraction of amblygonite-montebrasite, the O and H atoms have the largest scattering factors. From a practical standpoint, this means that these light elements are much more apparent on difference-Fourier maps, and occupancies and anisotropic displacement factors can be refined, which in general cannot be done with X-ray data. The main disadvantage of neutron relative to X-ray single-crystal diffraction is that the samples need to be substantially (~10×) larger. However, a single-crystal diffractometer (SCD) has been designed for the Spallation Neutron Source (SNS), which produces the most intense pulsed neutron beams in the world when completed in 2006. At SNS/SCD, it will be possible to collect data from much smaller crystals (<1 mm), and collection times for small molecule data will be reduced to minutes or a few hours, rather than days or weeks.

### EXPERIMENTAL METHODS

Four samples were used in the neutron diffraction study: “Dunton” is from the Dunton Gem Mine, Oxford County, Maine; “Tanco” is from the Tanco pegmatite, Bernic Lake, Manitoba; “AF-46” (U.S. National Museum of Natural History, no. 105914) is from Karibib, South Africa; and “Saxony” (California Institute of Technology no. 13696) is from the State of Saxony in Germany.

We had great difficulty finding a high-F sample. According to Groat et al. (1990), natural members of the series with F/(F + OH) > 0.65 are uncommon. The reason for this, as elucidated by London et al. (2001), is that most primary amblygonite-montebrasite contains ~4–7 wt% F, whereas end-member amblygonite contains approximately 13 wt% F. However, even the most-fractionated pegmatite melts contain no more than ~1.0–1.8 wt% F, as shown by the general lack of topaz in these rocks. In the topaz-bearing granites of western Europe, however, high-F amblygonite (~10–11 wt% F) is evidence of >3

wt% F in the melt during crystallization.

We spent a considerable amount of time trying to collect useful data from a fifth sample—“M6116” (Naturhistorisches Museum, Vienna; from Chursdorf, near Penig, Saxony, Germany), which was previously studied by Groat et al. (1990) and shown (from a structure refinement) to have F/(F + OH) = 0.86. However, in each case the quality of the data collected was poor and so were the resulting  $\chi^2$  and *R* values. In hand specimen, the material is translucent gray with white opaque regions that likely represent volumes with abundant veinlets of lacroixite (NaAlPO<sub>4</sub>F), as seen by Groat et al. (1990) in back-scattered electron images. Toward the end of the study, we obtained a cleavage fragment of the “Saxony” material. The new sample was pale greenish white and mostly opaque, with weakly translucent regions, and provided much better data.

We began by collecting powder neutron diffraction data at the High Flux Isotope Reactor (HFIR) at Oak Ridge National Laboratory. Data were collected for the Dunton and Tanco samples using a wavelength of 1.0037 Å at temperatures of 11 (Tanco only), 75, 150, 225, and 300 K. Refined lattice parameters (Table 1) were obtained using the General Structure Analysis System (GSAS) package of programs (Von Dreele and Larson 1998).

Samples were prepared for the single-crystal neutron diffraction study by grinding spheres approximately 2 mm in diameter. Data for all samples except Saxony were obtained using the four-circle diffractometer at HFIR; the wavelength was 1.0037 Å and  $\sin\Theta/\lambda = 0.98/\text{Å}$ . Half-spheres of data [corresponding to ~1000–1300 reflections, of which ~900–1200 had  $I > 3\sigma(I)$ ] were collected at temperatures of 15, 75, 150, 225, and 295 K for the Dunton and Tanco samples, and 12, 100, 200, and 295 K for AF-46. By the time we obtained a suitable high-F sample, the High Flux Reactor was shut down for extensive maintenance and instrument upgrades (which may include an upgraded monochromator for the single-crystal diffractometer that will increase the flux to the sample by an order of magnitude). However, we were able to collect low-temperature (20 K) time-of-flight neutron diffraction data from the Saxony sample with the single-crystal diffractometer at the Intense Pulsed Neutron Source (IPNS) at Argonne National Laboratory. Although the IPNS is a much less powerful source than HFIR, the time-of-flight technique allows more data to be collected simultaneously, so data collection rates are similar. A total of 1087 reflections were collected, 1076 of which had  $I > 3\sigma(I)$ .

An absorption correction was applied to all single-crystal neutron diffraction data. The neutron linear attenuation factor, which includes both incoherent scattering and absorption pro-

**TABLE 1.** Cell parameters from neutron powder diffraction data

Sample	<i>T</i> (K)	<i>a</i> (Å)	<i>b</i> (Å)	<i>c</i> (Å)	$\alpha$	$\beta$	$\gamma$	<i>V</i> (Å <sup>3</sup> )	( <i>V</i> - <i>V</i> <sub>295</sub> )/ <i>V</i> <sub>295</sub>
Dunton	295	6.7234(2)	7.7181(2)	7.0258(2)	91.302(1)	117.953(1)	91.773(2)	321.61(2)	0.0
	225	6.7198(2)	7.7149(2)	7.0249(2)	91.320(1)	117.953(1)	91.778(2)	321.25(2)	-0.24253
	150	6.7158(2)	7.7113(2)	7.0232(2)	91.343(1)	117.953(1)	91.778(2)	320.83(2)	-0.24253
	75	6.7129(2)	7.7095(2)	7.0231(2)	91.359(1)	117.960(1)	91.781(2)	320.59(2)	-0.31716
Tanco	295	6.6941(1)	7.7204(1)	6.9728(1)	90.919(1)	117.75(1)	91.369(1)	318.69(1)	0.0
	225	6.6914(1)	7.7150(1)	6.9697(1)	90.939(1)	117.76(1)	91.377(1)	318.17(1)	-0.16316
	150	6.6891(1)	7.7111(1)	6.9648(1)	90.958(1)	117.76(1)	91.382(1)	317.78(1)	-0.28554
	75	6.6871(1)	7.7085(1)	6.9660(1)	90.983(1)	117.76(1)	91.387(1)	317.49(1)	-0.37654
	11	6.6870(1)	7.7087(1)	6.9657(1)	90.990(1)	117.76(1)	91.385(1)	317.48(1)	-0.37968

cesses, ranges from 1.6, to 1.0, to 0.5 cm<sup>-1</sup> for pure montebrasite, a sample with equal amounts of F and OH, and pure amblygonite, respectively. The absorption is primarily due to the presence of <sup>6</sup>Li and the incoherent scattering is mainly due to the H atoms.

Structure refinements were done using the GSAS package of programs (Von Dreele and Larson 1998). The neutron scattering lengths used were 5.13(1) fm for P, 3.449(5) fm for Al, 5.803(4) fm for O, 5.654(10) fm for F, -3.7390(11) fm for H, and -1.90(2) fm for Li. Initial refinements were done using an isotropic model with ~37 variables; final refinements were done using an anisotropic model with 86–89 (HFIR data) or 125 (IPNS data) variables.

In their single-crystal XRD study, Groat et al. (1990) refined the position of the H atom in three samples with F/(F + OH) < 0.30. However, the occupancy and isotropic displacement parameters were fixed, the latter at  $U_{eq} = 0.01 \text{ \AA}^2$ . The Li1 and Li2 sites were constrained to be half-occupied and to have the same isotropic displacement factor. The advantage of the neutron diffraction data used in the present study is that it allowed us to refine the occupancies of the OH/F, H, Li1, and Li2 sites (the latter two constrained to total 1.0). Anisotropic displacement factors were used for all atoms except Li1 and Li2, for which isotropic displacement factors were refined independently. Miscellaneous information from data collection and refinement is given in Table 2; positional coordinates, equivalent isotropic displacement factors, and refined occupancies for OH/F, H, Li1, and Li2 are given in Tables 3–6; and interatomic distances and angles are listed in Tables 7–10.

For the NMR study, powders were prepared of the Dunton, Tanco, AF-46, and Saxony minerals, and also of the following samples [with F/(F + OH) values from Groat et al. 1990]: AF-43 (0.08), A-2 (0.30), and A-1 (0.45). High-resolution, solid-state NMR spectra were obtained using a Bruker AVANCE-400 spectrometer (9.4 T, 400 MHz proton resonance frequency) and a Varian Inova spectrometer (18.8 T, 800 MHz proton reso-

nance frequency) located at the Pacific Northwest National Laboratory, Richland, Washington (see Acknowledgments).

The <sup>6</sup>Li MAS NMR spectra at 9.4 T were obtained using a Bruker double-tuned CP (cross-polarization) MAS probe equipped with a 7 mm stator system from Doty Scientific and tuned to the <sup>6</sup>Li frequency at 58.88 MHz. The <sup>6</sup>Li MAS NMR spectra at 18.8 T were obtained using a homebuilt probe equipped with a 5 mm stator system from Doty Scientific and tuned to 117.76 MHz. All single-pulse <sup>6</sup>Li MAS NMR spectra were collected at spinning rates between 3 and 4 kHz, with a 45 degree pulse angle (pulse length of 4 μs) and a recycle delay of 900 s. The spectra at 9.4 T were collected with 40 scans whereas the spectra at 18.8 T were collected with 8 scans. All <sup>6</sup>Li NMR spectra were referenced with respect to 1 M aqueous LiCl solution.

The <sup>6</sup>Li{<sup>1</sup>H} and <sup>6</sup>Li{<sup>19</sup>F} CP and rotational-echo double-resonance (REDOR) experiments were obtained at 9.4 T using a Bruker CP MAS probe equipped with a 4 mm stator system at a spinning rate of 12 000 ± 5 Hz. Due to the isolated nature of the <sup>1</sup>H/<sup>6</sup>Li and <sup>19</sup>F/<sup>6</sup>Li spin pairs and the fast spinning rate, the CP matching condition was carefully set on the +1 spinning side band of the Hartmann-Hahn CP matching profile, such that  $\omega(^6\text{Li}) - \omega(^1\text{H}/^{19}\text{F}) = \omega_r$ , where  $\omega(^6\text{Li})$  and  $\omega(^1\text{H}/^{19}\text{F})$  are the radio frequency power levels for <sup>6</sup>Li and <sup>1</sup>H or <sup>19</sup>F, respectively, and  $\omega_r$  is the spinning rate. For <sup>6</sup>Li{<sup>1</sup>H} CP, the <sup>1</sup>H power was fixed at 48 kHz corresponding to a 90° pulse length of 5.2 ms, and the +1 CP match condition was found at a <sup>6</sup>Li power of 60 kHz corresponding to a 90° pulse length of 4.2 μs. For <sup>6</sup>Li{<sup>19</sup>F} CP, the +1 CP match condition was achieved with a <sup>19</sup>F power of 53 kHz (4.7 μs 90° pulse) and a <sup>6</sup>Li power of 65 kHz (3.8 μs 90° pulse). The CP experiments were performed with a recycle delay of ~1.25 ×  $T_1$  of <sup>1</sup>H or <sup>19</sup>F to achieve the maximum signal-to-noise ratio (S/N). The <sup>1</sup>H and <sup>19</sup>F  $T_1$  values of the samples across the amblygonite-montebrasite series, as measured by saturation recovery experiments, were as follows: Dunton -  $T_1(^1\text{H}) = 3.2 \text{ s}$ ; AF-43 -  $T_1(^1\text{H}) = 2.9 \text{ s}$ ,  $T_1(^{19}\text{F}) = 12 \text{ s}$ ;

TABLE 2. Data measurement and refinement information

	Dunton	Tanco	AF-46	Saxony	Saxony
T (K)	295	295	295	20	295 (X-ray)
a (Å)	6.7160(4)	6.6941(5)	6.6815(6)	6.678(3)	6.6603(4)
b (Å)	7.7173(7)	7.7110(6)	7.7160(6)	7.717(3)	7.7434(7)
c (Å)	7.0228(4)	6.9639(5)	6.9565(5)	6.931(3)	6.9319(4)
α (°)	91.250(6)	90.922(6)	90.777(6)	90.59(5)	90.392(8)
β (°)	117.913(4)	117.751(5)	117.617(6)	117.65(5)	117.432(5)
γ (°)	91.786(6)	91.415(6)	91.275(7)	91.08(4)	91.029(7)
V (Å <sup>3</sup> )	321.21(4)	317.87(4)	317.43(5)	316.3(3)	317.21(4)
Space Group	C $\bar{1}$	C $\bar{1}$	C $\bar{1}$	C $\bar{1}$	C $\bar{1}$
Z	4	4	4	4	4
F/(F + OH)*	0.04	0.45	0.55	0.77	0.77
Crystal dimensions or sphere radius (mm)	2.13	2.54	2.33 × 2.69 × 1.80	2.??	-
Scale factor	23.4(1)	27.1(1)	29.7(1)	*	-
Number of variables	88	86	89	125	-
Extinction coefficient (×10 <sup>-5</sup> )	4.2(2)	0.007(9)	3.5(2)	21(3)	-
Measured reflections	1024	1013	1261	1087	-
Reflections with I > 3σ(I)	922	934	1173	1076	-
Reduced χ <sup>2</sup>	2.61	1.99	2.36	2.02	-
R <sub>F</sub> %	4.2	2.2	2.5	8.6	-
wR <sub>F</sub> %	2.9	3.7	3.9	8.4	-
Weight	(2F <sub>o</sub> /σF <sub>o</sub> ) <sup>2</sup>	(2F <sub>o</sub> /σF <sub>o</sub> ) <sup>2</sup>	(2F <sub>o</sub> /σF <sub>o</sub> ) <sup>2</sup>	min(F <sub>o</sub> /F <sub>c</sub> , F <sub>o</sub> /F <sub>c</sub> ) <sup>4</sup> × [σF <sub>o</sub> <sup>2</sup> + (0.001 × F <sub>o</sub> ) <sup>2</sup> ]	-

Note: Refinement information based on single Li-site model. F/(F + OH) for AF-46 was given as 0.59 in Groat et al. (1990).

\*40 data histograms collected.

**TABLE 3.** Atomic parameters: Amblygonite-montebbrasite samples, Dunton (split Li-site model)

T(K)		15	75	150	225	295
P	x	0.9836(2)	0.9834(2)	0.9836(2)	0.9838(2)	0.9842(1)
	y	0.3424(2)	0.3420(1)	0.3421(2)	0.3422(1)	0.3422(1)
	z	0.2672(2)	0.2675(2)	0.2673(2)	0.2669(2)	0.2667(1)
	$U_{\text{eq}}$	0.32(4)	0.31(4)	0.38(5)	0.39(4)	0.50(3)
Al1	x	0	0	0	0	0
	y	0	0	0	0	0
	z	0	0	0	0	0
	$U_{\text{eq}}$	0.41(8)	0.33(7)	0.4(1)	0.43(7)	0.53(6)
Al2	x	0	0	0	0	0
	y	0	0	0	0	0
	z	$1/2$	$1/2$	$1/2$	$1/2$	$1/2$
	$U_{\text{eq}}$	0.27(8)	0.29(7)	0.4(1)	0.41(7)	0.52(6)
O1	x	-0.3180(2)	-0.3180(2)	-0.3182(2)	-0.3180(2)	-0.3175(2)
	y	0.0146(1)	0.0147(1)	0.0147(2)	0.0151(1)	0.0153(1)
	z	-0.1611(2)	-0.1610(2)	-0.1607(2)	-0.1603(2)	-0.1595(1)
	$U_{\text{eq}}$	0.45(4)	0.45(4)	0.60(5)	0.62(3)	0.77(3)
O2	x	0.2979(2)	0.2979(2)	0.2975(2)	0.2981(2)	0.2980(1)
	y	0.0589(1)	0.0589(1)	0.0586(2)	0.0587(1)	0.0583(1)
	z	0.5725(2)	0.5727(2)	0.5729(2)	0.5736(2)	0.5742(1)
	$U_{\text{eq}}$	0.44(4)	0.47(4)	0.56(5)	0.62(3)	0.76(3)
O3	x	0.1021(2)	0.1024(2)	0.1022(2)	0.1016(2)	0.1013(2)
	y	-0.2239(1)	-0.2237(1)	-0.2236(2)	-0.2236(1)	-0.2237(1)
	z	-0.3904(2)	-0.3900(2)	-0.3901(2)	-0.3899(1)	-0.3895(1)
	$U_{\text{eq}}$	0.45(4)	0.42(4)	0.51(5)	0.55(3)	0.70(3)
O4	x	0.0256(2)	0.0256(2)	0.0259(2)	0.0263(2)	0.0263(2)
	y	0.2357(1)	0.2358(1)	0.2360(2)	0.2360(1)	0.2360(1)
	z	0.1041(2)	0.1040(2)	0.1038(2)	0.1038(2)	0.1036(1)
	$U_{\text{eq}}$	0.48(4)	0.49(4)	0.64(5)	0.64(3)	0.81(3)
OH/F	x	0.0491(2)	0.0490(2)	0.0485(2)	0.0484(2)	0.0480(2)
	y	0.0894(1)	0.0896(1)	0.0894(2)	0.0893(1)	0.0893(1)
	z	-0.2255(2)	-0.2254(2)	-0.2257(2)	-0.2257(1)	-0.2258(1)
	$U_{\text{eq}}$	0.42(4)	0.44(4)	0.52(5)	0.52(3)	0.66(3)
H	x	0.2063(5)	0.2063(4)	0.2059(4)	0.2052(4)	0.2044(3)
	y	0.1337(3)	0.1336(3)	0.1335(4)	0.1336(3)	0.1335(3)
	z	0.8484(3)	0.8480(3)	0.8477(4)	0.8470(3)	0.8470(3)
	$U_{\text{eq}}$	1.7(1)	1.7(1)	1.9(1)	1.97(9)	2.07(8)
Li1	n	0.96(1)	0.95(1)	0.96(1)	0.98(1)	0.96(1)
	x	0.067(3)	0.061(3)	0.063(3)	0.064(5)	0.066(3)
	y	-0.323(2)	-0.322(2)	-0.322(2)	-0.317(3)	-0.317(2)
	z	0.322(3)	0.309(2)	0.303(3)	0.28(1)	0.274(7)
Li2	$U_{\text{iso}}$	0.7(4)	0.0(4)	0.1(4)	1.0(8)	1.3(5)
	n	0.50(7)	0.45(6)	0.39(5)	0.19(1)	0.23(7)
	x	0.070(3)	0.083(3)	0.077(3)	0.072(1)	0.0709(8)
	y	-0.320(2)	-0.321(2)	-0.320(2)	-0.3216(8)	-0.3213(5)
	z	0.305(3)	0.322(3)	0.325(2)	0.319(3)	0.318(2)
	$U_{\text{iso}}$	0.8(4)	1.8(4)	1.6(3)	1.0(2)	1.1(1)
	n	0.50(7)	0.55(6)	0.61(5)	0.81(1)	0.77(7)

Note:  $U$  values are listed  $\times 10^2 \text{ \AA}^2$ ;  $n$  = occupancy (when not listed, fixed at full occupancy).

A-1 –  $T_1(^1\text{H}) = 19$  s,  $T_1(^{19}\text{F}) = 22$  s; Saxony –  $T_1(^1\text{H}) = 3.3$  s,  $T_1(^{19}\text{F}) = 3.8$  s. Between 16 and 96 scans were collected for each CP spectrum.

The  $^6\text{Li}\{^1\text{H}\}$  and  $^6\text{Li}\{^{19}\text{F}\}$  REDOR experiments were performed as CP-REDOR experiments in which the initial  $90^\circ$  pulse on  $^6\text{Li}$  was replaced by  $^6\text{Li}\{^1\text{H}\}$  or  $^6\text{Li}\{^{19}\text{F}\}$  CP so that the recycle delay depended on the shorter  $T_1$  of  $^1\text{H}$  or  $^{19}\text{F}$  rather than the much longer  $T_1$  of  $^6\text{Li}$ . The CP match conditions and recovery times used in the CP-REDOR experiments were the same as described above. The  $^6\text{Li}$  refocusing  $180^\circ$  pulse applied after  $n/2$  rotor cycles was  $7.4 \mu\text{s}$ , and the rotor synchronized  $^1\text{H}$  or  $^{19}\text{F}$   $180^\circ$  dephasing pulses applied at every half and full rotor cycle were  $4.5 \mu\text{s}$  and  $5.6 \mu\text{s}$  respectively. The number of rotor periods  $n$  was incremented in steps of 2 to increase the dephasing time (dephasing time =  $n/\omega_r$ ). At each value of  $n$ , two spectra were collected: one with the dephasing pulses on  $^1\text{H}$  or  $^{19}\text{F}$  ( $S_d$ ), and one without the dephasing pulses ( $S_0$ ) to act as a reference spectrum. The effect of the dipolar dephasing is then shown by plotting the normalized difference spectra  $[\Delta S/$

$S_0 = (S_0 - S_d)/S_0]$  as a function of  $n$  or the dephasing time. Between 32 and 192 scans were collected for each CP-REDOR spectrum.

Peak areas were extracted from the  $^6\text{Li}$  spectra by deconvoluting the spectra into two Lorentzian peaks of equal line widths. This was done with in a program written in Mathematica version 3.0 (Wolfram 1996). The CP and REDOR curves were calculated and fit to the experimental data in a program also written in Mathematica with the equations previously used by Fyfe et al. (2001).

## RESULTS AND DISCUSSION

### Neutron diffraction

The refinement results show that the OH/F position is always fully occupied (Tables 3–6). The occupancy of the H site at 295 K for the Dunton, Tanco, and AF-46 samples is 0.96(1), 0.545(8), and 0.441(8), respectively; this feature is shown diagrammatically by the missing H atoms in Figures 1b and 1c.

**TABLE 4.** Atomic parameters: Amblygonite-montebbrasite samples, Tanco (split Li-site model)

T(K)		15	75	150	225	295
P	<i>x</i>	0.9846(2)	0.9845(2)	0.9846(1)	0.9847(1)	0.9851(1)
	<i>y</i>	0.3412(1)	0.3412(1)	0.3411(1)	0.3411(1)	0.3410(1)
	<i>z</i>	0.2625(1)	0.2624(1)	0.2620(1)	0.2616(1)	0.2618(1)
	$U_{\text{eq}}$	0.46(3)	0.47(3)	0.48(3)	0.56(3)	0.62(2)
Al1	<i>x</i>	0	0	0	0	0
	<i>y</i>	0	0	0	0	0
	<i>z</i>	0	0	0	0	0
	$U_{\text{eq}}$	0.46(7)	0.45(7)	0.49(6)	0.59(7)	0.63(5)
Al2	<i>x</i>	0	0	0	0	0
	<i>y</i>	0	0	0	0	0
	<i>z</i>	1/2	1/2	1/2	1/2	1/2
	$U_{\text{eq}}$	0.36(6)	0.38(7)	0.38(6)	0.47(6)	0.51(5)
O1	<i>x</i>	-0.3172(1)	-0.3171(1)	-0.3170(1)	-0.3168(1)	-0.3167(1)
	<i>y</i>	0.0150(1)	0.0148(1)	0.0153(1)	0.0159(1)	0.01652(7)
	<i>z</i>	-0.1547(1)	-0.1548(1)	-0.1541(1)	-0.1534(1)	-0.1526(1)
	$U_{\text{eq}}$	0.60(3)	0.61(3)	0.67(3)	0.78(3)	0.92(2)
O2	<i>x</i>	0.2982(1)	0.2980(1)	0.2984(1)	0.2984(1)	0.2985(1)
	<i>y</i>	0.0602(1)	0.0600(1)	0.0600(1)	0.0600(1)	0.05971(8)
	<i>z</i>	0.5794(1)	0.5792(1)	0.5798(1)	0.5802(1)	0.5808(1)
	$U_{\text{eq}}$	0.65(3)	0.66(3)	0.75(3)	0.84(3)	0.96(2)
O3	<i>x</i>	0.1013(1)	0.1010(1)	0.1008(1)	0.1004(1)	0.998(1)
	<i>y</i>	-0.2231(1)	-0.2231(1)	-0.2231(1)	-0.2229(1)	-0.22273(7)
	<i>z</i>	-0.3879(1)	-0.3880(1)	-0.3877(1)	-0.3873(1)	-0.3870(1)
	$U_{\text{eq}}$	0.54(3)	0.57(3)	0.62(3)	0.73(3)	0.83(2)
O4	<i>x</i>	0.0236(1)	0.0238(2)	0.0244(1)	0.0251(2)	0.0257(1)
	<i>y</i>	0.2337(1)	0.2338(1)	0.2339(1)	0.2338(1)	0.23365(8)
	<i>z</i>	0.0976(1)	0.0977(1)	0.0977(1)	0.0979(1)	0.0981(1)
	$U_{\text{eq}}$	0.65(3)	0.66(3)	0.75(3)	0.86(3)	0.99(2)
OH/F	<i>x</i>	0.0372(2)	0.0370(2)	0.0366(1)	0.0361(1)	0.0358(1)
	<i>y</i>	0.0865(1)	0.0865(1)	0.0865(1)	0.0866(1)	0.08658(8)
	<i>z</i>	-0.2318(1)	-0.2318(1)	-0.2320(1)	-0.2321(1)	-0.2324(1)
	$U_{\text{eq}}$	0.71(3)	0.72(3)	0.76(3)	0.84(3)	0.96(2)
H	<i>n</i>	1.003(7)	1.018(7)	1.006(7)	0.998(7)	0.994(5)
	<i>x</i>	0.2018(6)	0.2030(6)	0.2025(5)	0.2015(6)	0.2011(4)
	<i>y</i>	0.1370(4)	0.1371(5)	0.1370(4)	0.1370(5)	0.1373(3)
	<i>z</i>	0.8444(5)	0.8453(5)	0.8442(5)	0.8444(5)	0.8440(4)
Li1	$U_{\text{eq}}$	1.9(1)	1.9(1)	1.9(1)	2.0(1)	2.2(1)
	<i>n</i>	0.55(1)	0.55(1)	0.58(1)	0.55(1)	0.55(1)
	<i>x</i>	0.050(2)	0.047(2)	0.051(2)	0.052(2)	0.050(1)
	<i>y</i>	-0.323(1)	-0.323(1)	-0.3221(5)	-0.322(1)	-0.3230(8)
Li2	<i>z</i>	0.259(4)	0.259(4)	0.256(4)	0.252(3)	0.249(2)
	$U_{\text{iso}}$	1.2(3)	1.3(3)	1.4(3)	1.5(3)	1.7(2)
	<i>n</i>	0.38(5)	0.38(5)	0.36(4)	0.38(4)	0.37(3)
	<i>x</i>	0.068(1)	0.069(1)	0.0689(9)	0.0684(9)	0.0680(7)
Li2	<i>y</i>	-0.3215(6)	-0.3220(6)	-0.3220(5)	-0.3224(6)	-0.3218(4)
	<i>z</i>	0.315(2)	0.316(2)	0.316(2)	0.316(2)	0.316(1)
	$U_{\text{iso}}$	0.7(2)	0.7(2)	0.9(2)	0.9(2)	1.4(1)
	<i>n</i>	0.62(5)	0.61(5)	0.64(4)	0.62(4)	0.63(3)

Note:  $U$  values are listed  $\times 10^2 \text{ \AA}^2$ ;  $n$  = occupancy (when not listed, fixed at full occupancy).

The occupancies correspond to F/(F + OH) values of 0.04, 0.45, and 0.55; the latter is close to the value of 0.59 (average of four electron microprobe analyses) reported by Groat et al. (1990). The occupancy of the H site at 20 K for the Saxony sample is 0.23(1), which corresponds to an F/(F + OH) value of 0.77.

Variations in lattice parameters (single-crystals at 295 K; this study and Groat et al. 1990) as a function of F/(F + OH) are shown in Figure 2. The  $b$  parameter increases and  $a$ ,  $c$ , and  $V$  all decrease with increasing F/(F + OH). Groat et al. (1990) modeled the variation in  $V$  and  $b$  parameters with two linear segments meeting at approximately F/(F + OH) = 0.50 (variation in  $a$  and  $c$  was modeled as linear trends). They suggested that the inflection occurs at the same composition at which there is a break in the Li1-Li2 separation, and the nonlinear behavior of the cell volume with composition quantitatively accounts for the nonlinear variation in mean refractive index described by Greiner and Bloss (1987). However, in this study we chose to model the the variation in lattice parameters with shallow curves (although the  $c$  parameter appears to change linearly,

and the variation in the  $b$  parameter could be modeled with two linear segments), largely because of the paucity of data for higher values of F/(F + OH).

Although Cerná et al. (1973) and Groat et al. (1990) showed that lattice parameters vary as a function of F/(F + OH), they did not provide an explanation. We note that volume is highest for the OH end-member because of the presence of an additional atom (H). The  $a$  and  $c$  parameters decrease with increasing F/(F + OH) for two reasons: (1) the O-H vector is close to the  $\mathbf{a-c}$  plane; (2) the Al-OH/F bond distances decrease with increasing F/(F + OH) (as shown by Groat et al. 1990), and the Al-OH/F vectors are approximately parallel to  $\mathbf{c}$ .

In Figure 1, the structures of the Dunton, Tanco, and AF-46 samples are shown at 295 K. We note that the most obvious change with increasing F fraction is that the Li displacement ellipsoid becomes extremely large and anisotropic (as noted by Simonov and Belov 1958), which suggests that it actually represents two fractionally occupied positions. The displacement ellipsoids for the H atoms, however, show little change

**TABLE 5.** Atomic parameters: Amblygonite-montebbrasite samples, AF-46 (split Li-site model)

T(K)		12	100	200	295
P	x	0.9844(1)	0.9844(1)	0.9847(1)	0.98526(9)
	y	0.34096(9)	0.34098(9)	0.34071(8)	0.34060(7)
	z	0.2608(1)	0.2608(1)	0.2604(1)	0.26028(9)
	$U_{\text{eq}}$	0.41(3)	0.43(3)	0.59(3)	0.57(2)
Al1	x	0	0	0	0
	y	0	0	0	0
	z	0	0	0	0
	$U_{\text{eq}}$	0.36(6)	0.40(5)	0.51(5)	0.58(4)
Al2	x	0	0	0	0
	y	0	0	0	0
	z	$1/2$	$1/2$	$1/2$	$1/2$
	$U_{\text{eq}}$	0.31(6)	0.34(5)	0.41(5)	0.49(4)
O1	x	-0.3168(1)	-0.3167(1)	-0.3167(1)	-0.31648(8)
	y	0.01518(8)	0.01539(8)	0.01607(8)	0.01684(6)
	z	-0.1529(1)	-0.1526(1)	-0.1516(1)	-0.15047(9)
	$U_{\text{eq}}$	0.57(2)	0.59(2)	0.74(3)	0.88(2)
O2	x	0.2982(1)	0.2981(1)	0.2985(1)	0.29861(8)
	y	0.06035(9)	0.06028(9)	0.06010(8)	0.06004(7)
	z	0.5813(1)	0.5814(1)	0.5821(1)	0.58277(9)
	$U_{\text{eq}}$	0.61(2)	0.65(2)	0.79(2)	0.93(2)
O3	x	0.1009(1)	0.1007(1)	0.1003(1)	0.09968(8)
	y	-0.22275(8)	-0.22271(8)	-0.22251(8)	-0.22222(6)
	z	-0.3872(1)	-0.3870(1)	-0.3866(1)	-0.38606(8)
	$U_{\text{eq}}$	0.50(2)	0.54(3)	0.67(2)	0.79(2)
O4	x	0.0233(1)	0.0237(1)	0.0246(1)	0.02593(9)
	y	0.23330(9)	0.23331(9)	0.23318(8)	0.23308(7)
	z	0.0957(1)	0.0957(1)	0.0959(1)	0.09627(9)
	$U_{\text{eq}}$	0.61(3)	0.66(2)	0.82(2)	0.96(2)
OH/F	x	0.0333(1)	0.0331(1)	0.0325(1)	0.0318(1)
	y	0.08557(9)	0.08559(9)	0.08554(8)	0.08571(7)
	z	-0.2339(1)	-0.2341(1)	-0.2342(1)	-0.23449(9)
	$U_{\text{eq}}$	0.63(3)	0.67(3)	0.78(2)	0.87(2)
H	n	0.981(6)	0.980(6)	0.982(5)	0.979(4)
	x	0.2030(5)	0.2028(5)	0.2017(5)	0.2005(4)
	y	0.1376(5)	0.1371(5)	0.1370(4)	0.1377(3)
	z	0.8454(5)	0.8445(5)	0.8444(5)	0.8436(4)
Li1	$U_{\text{eq}}$	1.8(1)	1.8(1)	1.9(1)	2.2(1)
	n	0.44(1)	0.44(1)	0.44(1)	0.44(1)
	x	0.048(2)	0.050(1)	0.049(1)	0.047(1)
	y	-0.3214(9)	-0.3222(9)	-0.3214(8)	-0.3221(7)
Li2	z	0.254(3)	0.253(3)	0.250(2)	0.248(2)
	$U_{\text{iso}}$	0.7(3)	0.8(3)	1.3(2)	1.63(2)
	n	0.34(4)	0.35(4)	0.38(3)	0.40(3)
	x	0.0670(8)	0.0666(8)	0.0674(7)	0.0677(7)
$U_{\text{iso}}$	y	-0.3222(5)	-0.3227(5)	-0.3224(5)	-0.3234(5)
	z	0.313(2)	0.313(2)	0.313(1)	0.314(1)
	n	1.0(1)	1.1(1)	1.2(1)	1.56(5)
	n	0.65(4)	0.67(4)	0.62(3)	0.60(3)

Note:  $U$  values are listed  $\times 10^2 \text{ \AA}^2$ ;  $n$  = occupancy (when not listed, fixed at full occupancy).

with increasing F/(F + OH).

The low-temperature part of our study began with the collection of powder neutron diffraction data for the Dunton and Tanco samples, with F/(F + OH) = 0.04 and 0.45, respectively. The refined lattice parameters are given in Table 1. A graph of cell volume contraction (%) vs.  $T$  (K) (Fig. 3) shows that thermal contraction increases with F/(F + OH), presumably because the F anion takes up less space than the OH group.

The single-crystal neutron diffraction results show little change in occupancy values for both OH/F and H with decreasing temperature (Tables 3–6). As noted previously, Groat et al. (1990) showed that the Li atom is positionally disordered into two sites within this coordination. To investigate the nature of the disorder (static vs. dynamic), we collected neutron single-crystal diffraction data from several samples as a function of temperature. Figures 4 and 5 show equivalent isotropic  $U$  ( $\text{\AA}^2$ ) vs.  $T$  (K), single Li site model, for samples with different F/(F

**TABLE 6.** Atomic parameters: Amblygonite-montebbrasite samples, Saxony (split Li-site model)

T(K)		20		20	
P	x	-0.0154(2)	O4	x	0.0235(2)
	y	0.3404(1)		y	0.2326(1)
	z	0.2568(2)		z	0.0915(2)
	$U_{\text{eq}}$	0.75(5)		$U_{\text{eq}}$	0.96(5)
Al1	x	0	OH/F	X	0.0236(2)
	y	0		Y	0.0836(1)
	z	0		Z	-0.2390(2)
	$U_{\text{eq}}$	0.97(9)		$U_{\text{eq}}$	1.02(5)
Al2	x	0		N	0.28
	y	0	H	X	0.197(1)
	z	$1/2$		Y	0.140(1)
	$U_{\text{eq}}$	0.65(8)		z	0.838(1)
O1	x	-0.3160(2)		$U_{\text{eq}}$	2.0(4)
	y	0.0163(1)		n	0.23(1)
	z	-0.1479(2)	Li1	x	0.043(1)
	$U_{\text{eq}}$	0.91(5)		y	-0.3231(8)
O2	x	0.2987(1)		z	0.253(3)
	y	0.0610(1)		$U_{\text{iso}}$	1.7(2)
	z	0.5867(2)		n	0.64(7)
	$U_{\text{eq}}$	0.91(5)	Li2	x	0.069(3)
O3	x	0.0999(1)		y	-0.325(1)
	y	-0.2223(1)		z	0.307(5)
	z	-0.3845(2)		$U_{\text{iso}}$	1.0(3)
	$U_{\text{eq}}$	0.87(5)		n	0.36(7)

Note:  $U$  values are listed  $\times 10^2 \text{ \AA}^2$ ;  $n$  = occupancy (when not listed, fixed at full occupancy).

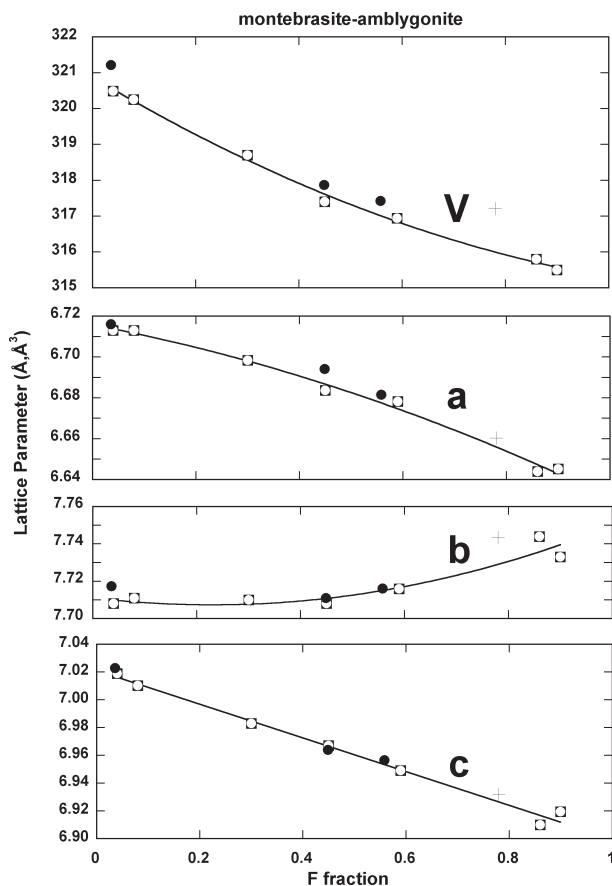


**FIGURE 2.** Lattice parameters ( $\text{\AA}$ ,  $\text{\AA}^3$ ) from single crystals at 295 K vs. F/(F + OH). The data are from the present study (neutron diffraction data shown as filled circles, X-ray data for the Saxony sample shown as crosses) and from Groat et al. (1990; X-ray diffraction data, shown as open circles).

**TABLE 7.** Interatomic distances (Å) in crystals of ambygonite-montebasite, Dunton (split Li-site model)

T(K)	15	75	150	225	295
P-O1a	1.531(1)	1.532(1)	1.532(1)	1.531(1)	1.534(1)
P-O2b	1.530(2)	1.531(1)	1.533(2)	1.529(1)	1.530(1)
P-O3c	1.543(2)	1.539(2)	1.541(2)	1.542(1)	1.541(1)
P-O4	1.529(2)	1.531(1)	1.530(1)	1.530(1)	1.531(1)
	1.533	1.533	1.534	1.533	1.534
Al1-O1 ×2	1.899(1)	1.899(1)	1.901(1)	1.9005(9)	1.8980(7)
Al1-O4 ×2	1.914(1)	1.915(1)	1.916(1)	1.9156(8)	1.9183(7)
Al1-OH ×2	1.901(1)	1.900(1)	1.900(1)	1.8995(9)	1.8992(7)
	1.905	1.905	1.906	1.9052	1.9051
Al2-O2 ×2	1.855(1)	1.855(1)	1.853(1)	1.856(1)	1.8541(8)
Al2-O3c ×2	1.9181(9)	1.9179(9)	1.917(1)	1.9167(8)	1.9186(6)
Al2-OHc ×2	1.904(1)	1.9062(9)	1.904(1)	1.9049(8)	1.9060(7)
	1.892	1.893	1.891	1.893	1.893
Li1-O1d	2.06(2)	2.04(2)	2.04(2)	2.06(2)	2.05(2)
Li1-O2e	2.05(1)	2.09(1)	2.10(2)	2.17(5)	2.17(3)
Li1-O3f	2.05(2)	2.18(9)	2.16(2)	2.31(8)	2.38(5)
Li1-O3g	2.06(2)	2.66(1)	2.05(2)	2.02(2)	2.02(2)
Li1-O4c	2.86(2)	2.774(1)	2.73(8)	2.56(9)	2.50(5)
Li1-OHc	1.99(1)	1.953(1)	1.95(2)	1.90(3)	1.92(2)
<Li1-O> 5	2.04	2.05	2.06	2.09	2.11
<Li1-O> 6	2.18	2.17	2.17	2.17	2.17
Li2-O1d	2.08(2)	2.134(1)	2.12(2)	2.089(6)	2.091(5)
Li2-O2e	2.09(2)	2.038(1)	2.05(1)	2.05(1)	2.056(5)
Li2-O3f	2.16(2)	2.083(1)	2.05(1)	2.08(2)	2.09(1)
Li2-O3g	2.00(2)	1.948(1)	1.99(2)	2.024(6)	2.033(5)
Li2-O4c	2.73(2)	2.824(1)	2.85(1)	2.82(2)	2.82(1)
Li2-OHc	1.96(2)	2.002(1)	1.99(1)	1.983(9)	1.980(5)
<Li2-O> 5	2.06	2.04	2.04	2.04	2.05
<Li1-O> 6	2.17	2.17	2.17	2.17	2.18
Li1-Li2	0.13(2)	0.13(2)	0.14(2)	0.26(7)	0.32(4)
H-OHf	0.977(3)	0.978(2)	0.979(3)	0.975(2)	0.974(2)
H-O4b	1.916(3)	1.914(3)	1.915(4)	1.916(2)	1.920(2)
OHf-O4b	2.849(2)	2.849(1)	2.850(2)	2.850(1)	2.852(1)
OHf-H-O4b	158.8(2)	159.0(2)	159.0(2)	159.5(2)	159.4(2)

Notes: a =  $1/2 - x - 1, 1/2 - y, -z$ ; b =  $1/2 - x, 1/2 - y, 1 - z$ ; c =  $-x, -y, -z$ ; d =  $1/2 - x - 1, 1/2 - y - 1, -z$ ; e =  $1/2 - x, 1/2 - y - 1, 1 - z$ ; f =  $x, y, z + 1$ ; g =  $1/2 - x, 1/2 - y - 1, -z$ .

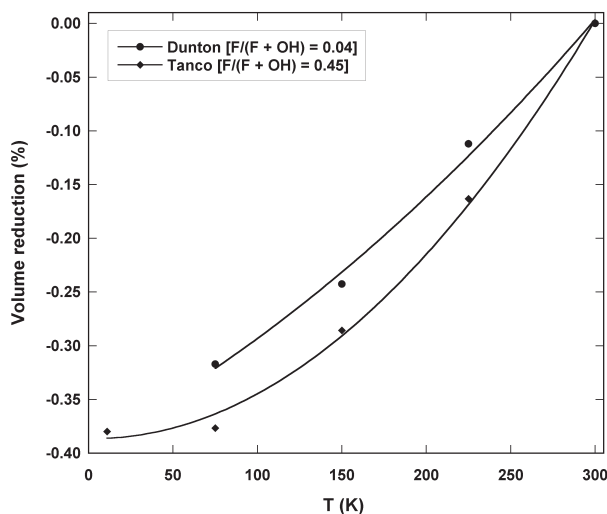


**FIGURE 3.** Cell volume contraction (%) vs.  $T$  (K) from powder neutron diffraction data for the Dunton and Tanco samples.

+ OH) values (Fig. 4 for all atoms, Fig. 5 for H and Li alone). The graphs show the following features: (1) the framework cations (Al1, Al2, and P) have the lowest  $U_{eq}$  values, and these vary little among samples and decrease only slightly with decreasing temperature; (2) the next highest atomic displacement parameters correspond to the oxygen atoms, and these show

little variation among samples and decrease only slightly with decreasing temperature; (3) the  $U_{eq}$  values corresponding to the H atom are much higher (approximately  $0.02 \text{ \AA}^2$  at 295 K) but vary little among samples, and decrease only slightly with decreasing temperature; and (4) the  $U_{eq}$  values at 295 K corresponding to the Li atom increase dramatically with  $F/(F + OH)$  and show a greater reduction with decreasing temperature than the other atoms. The fact that the curves are the same shape shows that the temperature dependence of Li is the same regardless of F content. However, the increasing positional disorder of the Li atom results in the curves shifting upward. The large intercepts at zero temperature for the Li atomic displacement parameter imply a large static disorder. Without any static disorder, the zero temperature values would be proportional to the quantum mechanical zero-point vibration.

Figure 6 shows  $U_1$ ,  $U_2$ , and  $U_3$  vs.  $T$  (K) for anisotropic Li in the Tanco sample, single Li site model. The graph shows that most of the distortion is associated with the  $U_3$  eigenvalue, which lies between the  $c$  and  $c^*$  directions.

Li- $\phi$  ( $\phi = O, OH, F$ ) and Li-H distances (single Li site model) are shown as a function of F fraction in Figure 7. This graph shows five short and one very long (Li-O4) bond at the montebasite end; with increasing F content, the Li-O4 distance decreases and the Li-O3f distance increases, such that at the ambygonite end, the coordination is  $4 + 2$ . The disorder in the Li site is obviously caused by the substitution of F for OH. The driving force is the loss of the hydrogen bond to O4, which causes the Li-O4 bond to strengthen and improves the bond

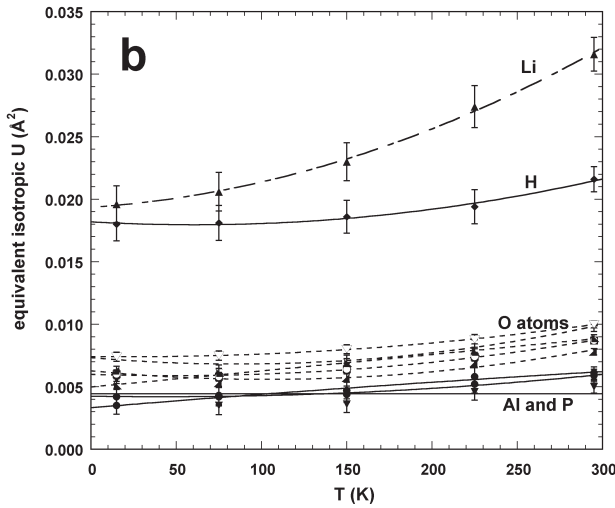
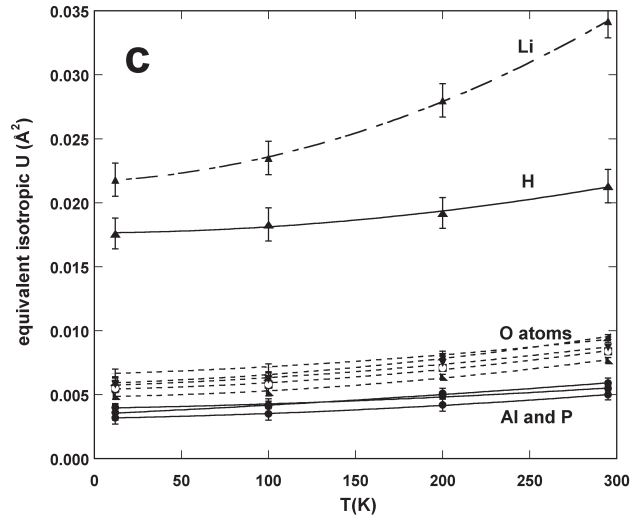
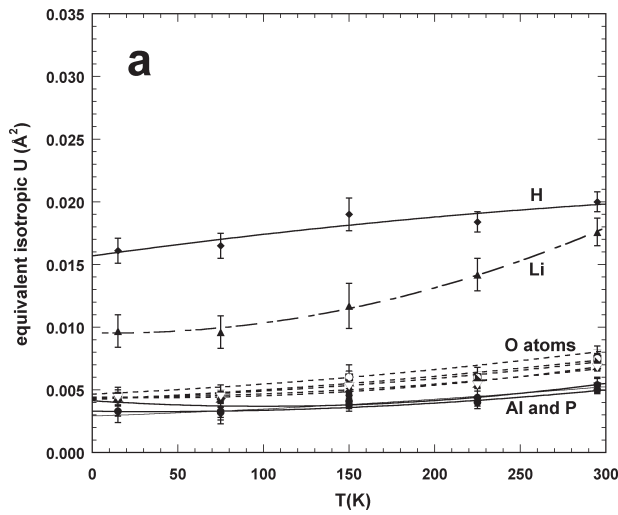


FIGURE 4. Equivalent isotropic atomic displacement factors  $U$  ( $\text{\AA}^2$ ) as a function of  $T$  (K) from single-crystal neutron diffraction data for (a) Dunton mine, (b) Tanco mine, and (c) AF-46.

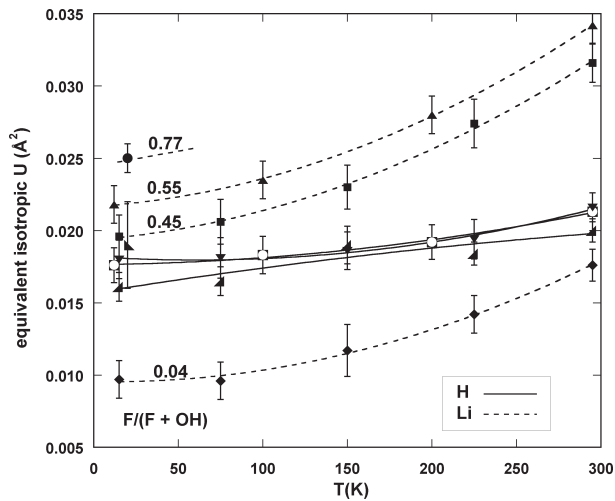


FIGURE 5. Equivalent isotropic atomic displacement factors  $U$  ( $\text{\AA}^2$ ) for H and Li atoms as a function of  $T$  (K) and OH content (single-crystal neutron diffraction data).

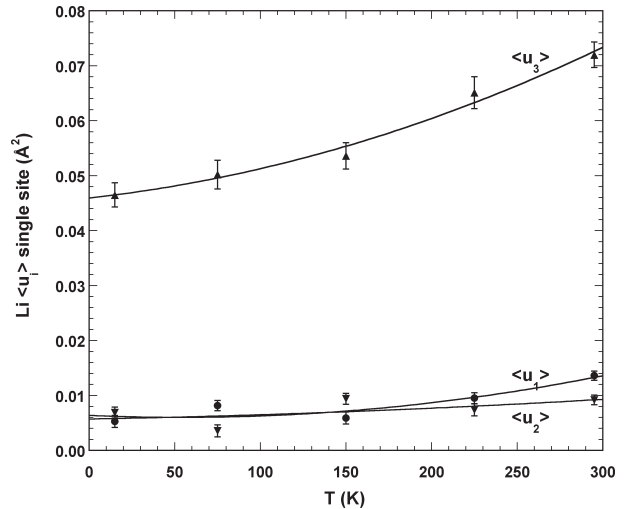


FIGURE 6. Temperature dependence of the eigenvalues for the Li atomic displacement parameter ellipsoids  $\text{Li } \langle u_i \rangle$  (single-site model) for the Tanco sample.

**TABLE 8.** Interatomic distances (Å) in crystals of amblygonite-montebbrasite, Tanco (split Li-site model)

T (K)	15	75	150	225	295
P-O1a	1.532(1)	1.533(1)	1.532(1)	1.530(1)	1.5319(8)
P-O2b	1.525(1)	1.526(1)	1.526(2)	1.526(1)	1.5249(9)
P-O3c	1.546(1)	1.544(1)	1.546(1)	1.545(1)	1.5418(9)
P-O4	1.525(1)	1.525(1)	1.524(1)	1.523(1)	1.5257(9)
	1.532	1.532	1.532	1.531	1.531
Al1-O1 ×2	1.8860(8)	1.8861(9)	1.8866(8)	1.8859(9)	1.8868(6)
Al1-O4 ×2	1.8888(8)	1.8899(8)	1.8921(8)	1.8913(8)	1.8915(6)
Al1-OH ×2	1.8743(9)	1.8738(9)	1.8747(8)	1.8734(9)	1.8734(7)
	1.8831	1.8833	1.8844	1.8835	1.8839
Al2-O2 ×2	1.8478(9)	1.8464(9)	1.8496(9)	1.8491(9)	1.850(7)
Al2-O3c ×2	1.9050(8)	1.9055(8)	1.9064(7)	1.9042(8)	1.904(6)
Al2-OHc ×2	1.8728(8)	1.8730(8)	1.8736(8)	1.8751(8)	1.874(6)
	1.8752	1.8750	1.8764	1.8761	1.876
Li1-O1d	1.989(1)	1.970(1)	1.996(1)	2.00(1)	1.999(8)
Li1-O2e	2.177(1)	2.180(1)	2.184(1)	2.18(1)	2.091(8)
Li1-O3f	2.421(2)	2.427(2)	2.445(2)	2.48(2)	2.50(1)
Li1-O3g	2.086(1)	2.107(1)	2.087(1)	2.077(1)	2.094(8)
Li1-O4c	2.413(2)	2.410(2)	2.388(2)	2.360(2)	2.35(1)
Li1-OHc	1.907(8)	1.907(9)	1.908(9)	1.913(8)	1.915(6)
<Li1-O> 5	2.114	2.115	2.112	2.108	2.089
<Li1-O> 6	2.165	2.166	2.169	2.171	2.158
Li2-O1d	2.088(6)	2.090(7)	2.094(6)	2.095(6)	2.101(4)
Li2-O2e	2.053(5)	2.048(6)	2.051(5)	2.047(5)	2.051(4)
Li2-O3f	2.095(1)	2.098(1)	2.100(1)	2.107(1)	2.109(7)
Li2-O3g	2.042(5)	2.036(5)	2.045(5)	2.051(5)	2.058(4)
Li2-O4c	2.749(1)	2.749(1)	2.750(1)	2.750(1)	2.749(7)
Li2-OHc	1.959(5)	1.963(5)	1.961(5)	1.961(5)	1.957(4)
<Li2-O> 5	2.047	2.047	2.050	2.052	2.055
<Li2-O> 6	2.164	2.164	2.166	2.161	2.171
Li1-Li2	0.35(1)	0.359(1)	0.377(4)	0.40(1)	0.419(9)
H-OHf	1.035(3)	1.043(4)	1.043(3)	1.040(3)	1.041(3)
H-O4b	1.932(4)	1.924(4)	1.925(4)	1.927(4)	1.925(3)
OHf-O4b	2.934(1)	2.933(1)	2.936(1)	2.935(1)	2.935(1)
OHf-H-O4b	162.3(3)	162.0(3)	162.2(3)	162.3(3)	162.3(2)

Note: a =  $\frac{1}{2} - x - 1, \frac{1}{2} - y, -z$ ; b =  $\frac{1}{2} - x, \frac{1}{2} - y, 1 - z$ ; c =  $-x, -y, -z$ ; d =  $\frac{1}{2} - x - 1, \frac{1}{2} - y - 1, -z$ ; e =  $\frac{1}{2} - x, \frac{1}{2} - y - 1, 1 - z$ ; f =  $x, y, z + 1$ ; g =  $\frac{1}{2} - x, \frac{1}{2} - y - 1, -z$ .

**TABLE 10.** Interatomic distances (Å) in crystals of amblygonite-montebbrasite, Saxony (split Li-site model)

T (K)	20	20	
P-O1a	1.528(2)	Li2-O1d	2.10(2)
P-O2b	1.528(2)	Li2-O2e	2.03(1)
P-O3c	1.545(2)	Li2-O3f	2.19(3)
P-O4	1.529(2)	Li2-O3g	2.04(1)
	1.533	Li2-O4c	2.64(3)
Al1-O1 ×2	1.878(2)	Li2-OHc	1.96(1)
Al1-O4 ×2	1.877(1)	<Li2-O> 5	2.06
Al1-OH ×2	1.856(1)	<Li2-O> 6	2.16
	1.870	Li1-Li2	0.33(1)
Al2-O2 ×2	1.846(1)	H-OHf	1.104(8)
Al2-O3c ×2	1.901(1)	H-O4b	1.940(8)
Al2-OHc ×2	1.850(1)	OHf-O4b	3.024(2)
	1.866	OHf-H-O4b	166.4(7)
Li1-O1d	1.979(8)		
Li1-O2e	2.18(1)		
Li1-O3f	2.48(2)		
Li1-O3g	2.142(9)		
Li1-O4c	2.33(2)		
Li1-OHc	1.903(6)		
5	2.11		
6	2.17		

Note: a =  $\frac{1}{2} - x - 1, \frac{1}{2} - y, -z$ ; b =  $\frac{1}{2} - x, \frac{1}{2} - y, 1 - z$ ; c =  $-x, -y, -z$ ; d =  $\frac{1}{2} - x - 1, \frac{1}{2} - y - 1, -z$ ; e =  $\frac{1}{2} - x, \frac{1}{2} - y - 1, 1 - z$ ; f =  $x, y, z + 1$ ; g =  $\frac{1}{2} - x, \frac{1}{2} - y - 1, -z$ .

valence to O4. The results show that the H atom position is imbedded *within* the distorted octahedral oxygen coordination of the Li atom. The Li-H distance is actually shorter than the two longest Li-O distances (Li-O4 and Li-O3f) for the Dunton, Tanco, and AF-46 samples, and is shorter than all but Li-O1

**TABLE 9.** Interatomic distances (Å) and angles (°) in crystals of amblygonite-montebbrasite, AF-46 (split Li-site model)

T (K)	12	100	200	295
P-O1a	1.531(1)	1.531(1)	1.5300(9)	1.5307(8)
P-O2b	1.528(1)	1.529(1)	1.5281(9)	1.5261(8)
P-O3c	1.546(1)	1.545(1)	1.5440(9)	1.5433(7)
P-O4	1.526(1)	1.529(1)	1.5284(9)	1.5284(8)
	1.533	1.534	1.5326	1.5321
Al1-O1 ×2	1.8825(7)	1.8817(7)	1.8826(6)	1.8826(5)
Al1-O4 ×2	1.8848(7)	1.8863(7)	1.8856(6)	1.8865(5)
Al1-OH ×2	1.8676(7)	1.8684(7)	1.8672(7)	1.8680(6)
	1.8783	1.8787	1.8785	1.8790
Al2-O2 ×2	1.8454(7)	1.8443(7)	1.8465(6)	1.8470(5)
Al2-O3c ×2	1.9013(7)	1.9015(7)	1.9005(6)	1.8998(5)
Al2-OHc ×2	1.8654(7)	1.8656(7)	1.8673(7)	1.8680(5)
	1.8707	1.8705	1.8714	1.8716
Li1-O1d	1.989(8)	1.996(7)	2.003(7)	1.997(6)
Li1-O2e	2.19(1)	2.19(1)	2.197(9)	2.199(8)
Li1-O3f	2.46(2)	2.46(2)	2.50(1)	2.51(1)
Li1-O3g	2.102(8)	2.091(7)	2.095(7)	2.113(6)
Li1-O4c	2.36(2)	2.35(2)	2.33(1)	2.33(1)
Li1-OHc	1.896(7)	1.906(7)	1.900(6)	1.901(6)
<Li1-O> 5	2.11	2.11	2.11	2.11
<Li1-O> 6	2.17	2.17	2.18	2.18
Li2-O1d	2.086(5)	2.085(5)	2.095(4)	2.101(4)
Li2-O2e	2.053(5)	2.051(5)	2.048(4)	2.039(4)
Li2-O3f	2.118(9)	2.121(9)	2.126(8)	2.129(7)
Li2-O3g	2.050(4)	2.054(4)	2.054(4)	2.060(4)
Li2-O4c	2.72(1)	2.72(1)	2.720(9)	2.730(8)
Li2-OHc	1.954(5)	1.956(4)	1.955(4)	1.963(4)
<Li2-O> 5	2.052	2.052	2.056	2.058
<Li2-O> 6	2.164	2.165	2.166	2.170
Li1-Li2	0.37(1)	0.381(9)	0.400(8)	0.416(7)
H-OHf	1.067(3)	1.067(3)	1.064(3)	1.063(2)
H-O4b	1.926(3)	1.925(3)	1.928(3)	1.926(3)
OHf-O4b	2.961(1)	2.960(1)	2.960(1)	2.958(8)
OHf-H-O4b	162.3(3)	162.4(3)	162.4(3)	162.8(2)

Note: a =  $\frac{1}{2} - x - 1, \frac{1}{2} - y, -z$ ; b =  $\frac{1}{2} - x, \frac{1}{2} - y, 1 - z$ ; c =  $-x, -y, -z$ ; d =  $\frac{1}{2} - x - 1, \frac{1}{2} - y - 1, -z$ ; e =  $\frac{1}{2} - x, \frac{1}{2} - y - 1, 1 - z$ ; f =  $x, y, z + 1$ ; g =  $\frac{1}{2} - x, \frac{1}{2} - y - 1, -z$ .

and Li-OH/F for the Saxony sample. The Li-H distance in all of the samples is only marginally longer than that observed in lithium hydride (2.030–2.042 Å; Vidal and Vidal-Valat 1986; Calder et al. 1962).

As done by Groat et al. (1990), we used a split Li site model to model the disorder better (Fig. 8). Figure 9 shows that Li1 occupancy increases and the Li2 occupancy decreases with increasing F content. Figure 9 also shows that the Li1-Li2 distance is longer for intermediate compositions [0.420(9) Å for the Tanco crystal and 0.416(7) Å for the AF-46 material] than for the end-members [0.32(4) Å for the Dunton sample and 0.33(1) Å for the Saxony amblygonite]. This result is somewhat different than Figure 4f in Groat et al. (1990), which shows the Li1-Li2 distance increasing from ~0.2 Å at F/(F + OH) = 0 to ~0.4 Å at an F fraction of approximately 0.50, then staying constant to the amblygonite end of the series.

### Nuclear magnetic resonance

In a previous study, Groat et al. (1990) collected MAS NMR spectra for selected nuclei for several amblygonite-montebbrasite samples across the series. Each sample gave a single broad resonance at –15.8 ppm in its  $^{31}\text{P}$  MAS NMR spectra that showed no change with composition, in line with the unchanging local environment of the  $^{31}\text{P}$  nuclei across the series. Although there are two Al sites in members of the amblygonite-montebbrasite series, the  $^{27}\text{Al}$  MAS NMR spectra showed only one broad peak,

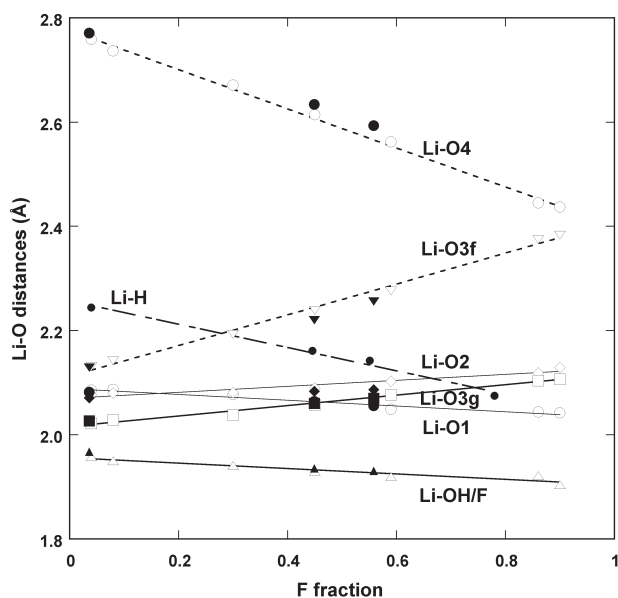


FIGURE 7. Variation of Li-O, Li-OH/F, and Li-H distances (Å) with F content for the single Li-site model. The solid symbols are from single-crystal neutron data in this study, and the open symbols are from the single-crystal X-ray study of Groat et al. (1990).

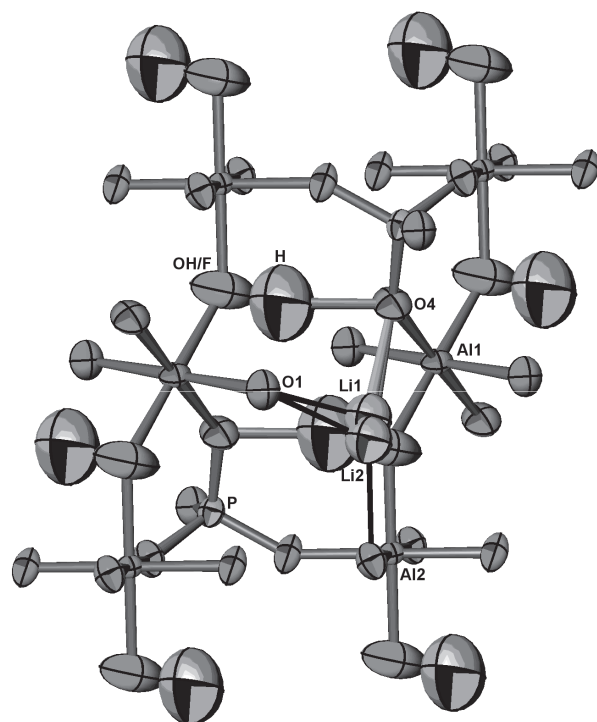


FIGURE 8. ORTEP diagram showing the H-O4 bond and the split Li position in amblygonite-montebbrasite.

reflecting the similarity of the two Al sites. As  $F/(F + OH)$  increased, the  $^{27}\text{Al}$  spectra shifted to lower field and the peak width decreased slightly, probably as a result of a decrease in dipolar coupling between the proton and Al with decreasing

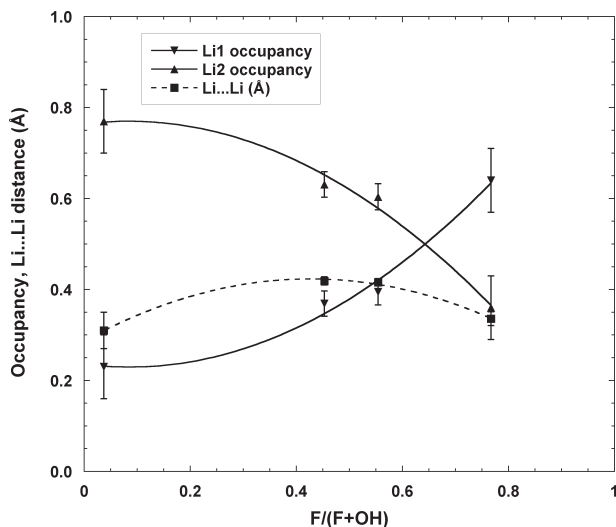


FIGURE 9. Li1 and Li2 occupancy and Li1-Li2 distance (Å) as a function of  $F/(F + OH)$ .

OH content. The  $^{19}\text{F}$  MAS NMR spectra of the samples across the series consisted of an isotropic chemical shift at  $-146$  ppm with many spinning sidebands, reflecting the large chemical shift anisotropy that arises from the F being in an anisotropic environment of threefold coordination (two Al and one Li).  $^6\text{Li}$  and  $^7\text{Li}$  spectra also were collected, but they did not provide evidence for the existence of more than one type of Li site as only one peak was observed in all spectra.

With improvement in NMR instrumentation, particularly the availability of very high field magnets, digital control of resonance frequency, and the development of solid-state NMR techniques to measure internuclear distances, a comprehensive series of  $^6\text{Li}$  and  $^7\text{Li}$  NMR experiments have been carried out to obtain information about the Li sites in the amblygonite-montebbrasite series to complement the neutron diffraction results presented above.

$^7\text{Li}$  ( $I = 3/2$ ) is typically the isotope of choice to study Li by NMR due to its greater sensitivity over  $^6\text{Li}$  ( $I = 1$ ) arising from its higher natural abundance (7.4%  $^6\text{Li}$ , 92.6%  $^7\text{Li}$ ), much larger magnetogyric ratio, and typically shorter  $T_1$  relaxation times. Both nuclei suffer from a narrow isotropic chemical shift range, however, because the quadrupolar interactions for  $^7\text{Li}$  are about 50 times larger than for  $^6\text{Li}$  and there typically exists some residual  $^7\text{Li}$ - $^7\text{Li}$  dipolar couplings due to the high  $^7\text{Li}$  natural abundance and large magnetogyric ratio of  $^7\text{Li}$ , it is especially difficult to obtain  $^7\text{Li}$  spectra with high chemical shift resolution. On the other hand, although it is more likely to obtain high resolution in  $^6\text{Li}$  spectra due to the much smaller quadrupolar interactions, the low natural abundance, low magnetogyric ratio, and longer  $T_1$  relaxation times mean that obtaining suitable S/N in  $^6\text{Li}$  MAS NMR spectra may well present a significant challenge. However, performing the NMR experiments at higher magnetic fields predictably increases the S/N and, in many cases, the resolution.

The  $^7\text{Li}$  MAS NMR spectra obtained at magnetic fields of 9.4 T and 18.8 T ( $^7\text{Li}$  frequencies of 155.54 and 311.08 MHz)

still show no evidence of more than one Li site in either the isotropic resonance or the satellite transitions. However, with careful adjustment of the shim settings (to ensure optimum magnetic field homogeneity over the whole sample volume) and the precise setting of the magic angle, the  ${}^6\text{Li}$  MAS NMR spectra of the series show two peaks at  $-0.3$  ppm and  $-0.9$  ppm at both 9.4 T and 18.8 T ( ${}^6\text{Li}$  frequencies of 58.88 and 117.76 MHz) as shown in Figure 10, confirming the existence of two Li sites as suggested by the neutron and X-ray diffraction data. These spectra also demonstrate the notable gain in resolution achievable at very high magnetic field strength.

Furthermore, the relative intensities of the two peaks in the  ${}^6\text{Li}$  MAS NMR spectra reflect the relative amount of F and OH found in the sample. As  $F/(F + \text{OH})$  increases, the intensity of the peak at  $-0.9$  ppm increases relative to the peak at  $-0.3$  ppm. Based on this observation, the peak at  $-0.9$  ppm can be assigned to Li1(F) and the peak at  $-0.3$  ppm to Li2(OH). The numbers to the right of each spectrum in Figure 10 are the Li1/(Li1 + Li2) values determined by deconvoluting the spectra with two Lorentzian peaks of equal width. Because each Li1 atom is bonded to F and each Li2 bonded to OH, this ratio is equivalent to  $F/(F + \text{OH})$ . Table 11 shows that these ratios determined by NMR are in good agreement with the ratios determined from the H occupancies in the neutron diffraction refinements and from the microprobe analyses (Groat et al. 1990). Small differences in the  $F/(F + \text{OH})$  ratios are expected due to different sample sizes and their heterogeneous nature.

Xu and Stebbins (1995) have shown that the isotropic chemical shifts of  ${}^6\text{Li}$  in crystalline and glassy silicates reflect the

coordination of the Li sites. They observed that the  ${}^6\text{Li}$  isotropic chemical shift is shifted downfield (to more negative values) as the coordination of the Li site increases. The Li- $\phi$  ( $\phi = \text{O, OH, F}$ ) distances determined by neutron diffraction (see Fig. 7) indicate that the Li1(F) site ( $-0.9$  ppm) is sixfold-coordinate and the Li2(OH) site ( $-0.3$  ppm) is fivefold-coordinate, suggesting that these  ${}^6\text{Li}$  isotropic chemical shifts may indeed arise from the different coordinations of the two Li sites.

It is important to establish the quantitative reliability of these  ${}^6\text{Li}$  MAS NMR spectra. Preliminary experiments using a wide range of delay times established that the  ${}^6\text{Li}$  nuclei in the two sites have very similar  $T_1$  values as their relative intensities were unchanged. The results of a detailed  ${}^6\text{Li}$  saturation recovery  $T_1$  experiment on sample A-1 at 9.4 T are shown in Figure 11 in which the peak areas for the two peaks are plotted as a function of recovery time. These data indicate that the two peaks have identical spin-lattice relaxation behaviors with a long  $T_1$  value of about 1600 s. Although the  $T_1$  relaxation times of  ${}^6\text{Li}$  are very long and may possibly vary from sample to sample as the levels of trace impurities vary, these results show that the relaxation behavior of the two  ${}^6\text{Li}$  sites are the same. It is there-

**TABLE 11.** Comparison of  $F/(F + \text{OH})$  ratios determined by electron microprobe analysis, neutron diffraction, and by  ${}^6\text{Li}$  MAS NMR

Sample	Electron microprobe*	Neutron diffraction†	${}^6\text{Li}$ NMR (9.4 T)‡	${}^6\text{Li}$ NMR (18.8 T)‡
Dunton	0.04	0.04	0.06	0.04
AF-43	0.08	—	0.16	0.16
A-2	0.30	—	0.42	0.37
A-1	0.45	—	0.51	0.50
Tanco	—	0.45	0.51	0.49
AF-46	0.59	0.55	0.57	0.60
Saxony	—	0.77	0.59	0.63

\* From Groat et al. (1990).

† From the occupancy of the H site from the refinements of the neutron diffraction data at 295 K (except Saxony, 20 K).

‡ From deconvolution of the  ${}^6\text{Li}$  MAS NMR spectra with Lorentzian peaks of equal width (see Fig. 10).

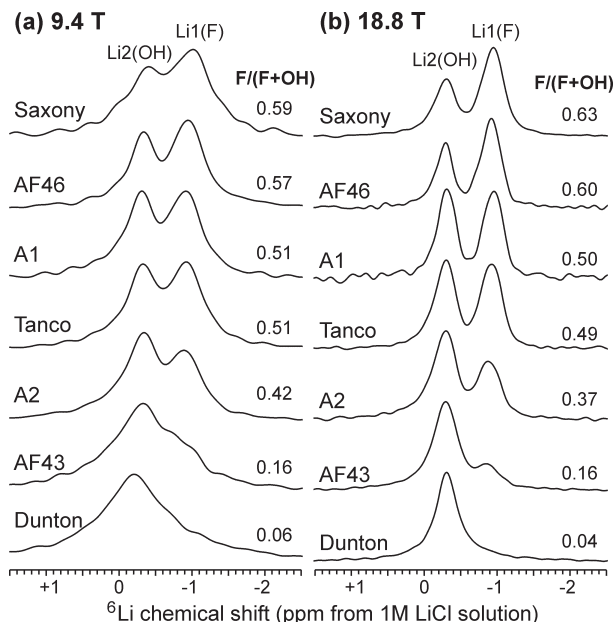


**FIGURE 10.**  ${}^6\text{Li}$  MAS NMR spectra of the ambygonite-montebasite series of samples at (a) 9.4 T ( ${}^6\text{Li}$  frequency = 58.88 MHz) and (b) 18.8 T ( ${}^6\text{Li}$  frequency = 117.76 MHz). The numbers to the right of each spectrum indicate the  $F/(F + \text{OH})$  ratio as determined from the deconvolution of the spectra with Lorentzian peaks of equal width.

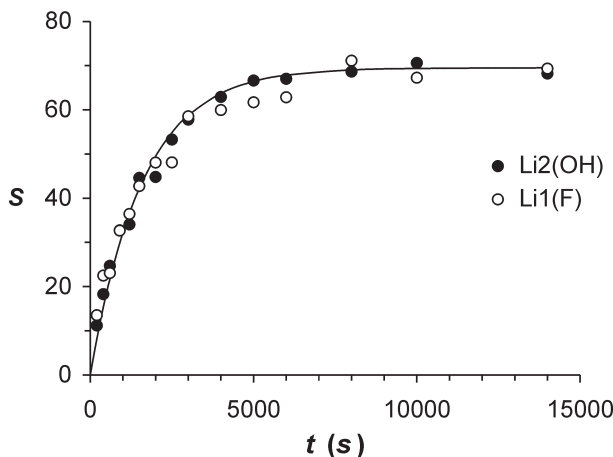


**FIGURE 11.**  ${}^6\text{Li}$  saturation recovery experiment on sample A-1 in which deconvoluted peak areas are plotted as a function of recovery time. The solid line is calculated with  $T_1 = 1600$  s. Two scans were collected for each spectrum.

fore safe to assume that the relative intensities of the two peaks in all the samples are quantitatively reliable.

Harris and Minoja (1995) and Penner and Hutzel (1997) have reported that the S/N of  ${}^6\text{Li}$  NMR spectra can be improved significantly by performing  ${}^6\text{Li}\{^1\text{H}\}$  CP MAS experiments because the recycle delay depends on the typically faster relaxing  ${}^1\text{H}$  nuclei and there is an enhancement factor of up to  $\gamma(^1\text{H})/\gamma(^{19}\text{F}) = 6.8$ . As there is more than one Li site in the amblygonite-montebbrasite structures,  ${}^6\text{Li}\{^1\text{H}\}$  and  ${}^6\text{Li}\{^{19}\text{F}\}$  CP MAS NMR can be extended beyond simple S/N enhancement to obtain qualitative and even quantitative structural information. In a CP experiment between nucleus  $I$  ( ${}^1\text{H}$  or  ${}^{19}\text{F}$ ) and nucleus  $S$  ( ${}^6\text{Li}$ ), magnetization is transferred from the  $I$  nuclei to the  $S$  nuclei in a distance dependent manner facilitated by the  $I$ - $S$  dipolar couplings. The result is an enhanced signal for those  $S$  nuclei that are closest to the source  $I$  nuclei. In addition to this qualitative structural information, it is possible to obtain quantitative structural information in the form of  $I$ - $S$  dipolar couplings (and thus  $I$ - $S$  internuclear distances) when there are isolated  $I$ - $S$  spin pairs.

A complementary NMR experiment to CP, in terms of obtaining structural information, is the REDOR experiment (Guillion and Schaefer 1989a, 1989b). In the REDOR experiment, the dipolar couplings that exist between the  $I$  and  $S$  nuclei, which are normally removed under MAS conditions, are reintroduced in a manner that causes dipolar dephasing of the  $S$  nuclei that have dipolar couplings to  $I$  nuclei. The result is a loss of signal for those  $S$  nuclei close to the  $I$  nuclei. When isolated  $I$ - $S$  spin pairs exist, it is also possible to measure  $I$ - $S$  internuclear distances by REDOR.

We have used  ${}^{29}\text{Si}\{^{19}\text{F}\}$  CP and REDOR experiments to measure F-Si distances in various zeolite materials (Fyfe et al. 1997, 1999, 2001, 2002). Further details about the CP and REDOR NMR experiments can be found in those papers and in their references. To the best of our knowledge,  ${}^6\text{Li}\{^1\text{H}\}$  and  ${}^6\text{Li}\{^{19}\text{F}\}$  CP and REDOR experiments never have been used to obtain qualitative structural information and internuclear distances.

Further evidence for the assignment of the two  ${}^6\text{Li}$  peaks is provided by  ${}^6\text{Li}\{^1\text{H}\}$  and  ${}^6\text{Li}\{^{19}\text{F}\}$  CP and REDOR experiments. In Figure 12, the results of  ${}^6\text{Li}\{^1\text{H}\}$  and  ${}^6\text{Li}\{^{19}\text{F}\}$  CP and REDOR experiments on sample A-1, with  $F/(F + \text{OH}) = 0.5$ , are presented. In the  ${}^6\text{Li}\{^1\text{H}\}$  CP and spectrum, the peak at  $-0.3$  ppm is enhanced whereas in the  ${}^6\text{Li}\{^{19}\text{F}\}$  CP spectrum, the peak at  $-0.9$  ppm is enhanced. Likewise in the  ${}^6\text{Li}\{^1\text{H}\}$  REDOR experiment, the peak at  $-0.3$  ppm is dephased whereas in the  ${}^6\text{Li}\{^{19}\text{F}\}$  REDOR experiment, the peak at  $-0.9$  ppm is dephased. These results clearly demonstrate that the peak at  $-0.9$  ppm is Li1(F) and the peak at  $-0.3$  ppm is Li2(OH).

In addition to the  ${}^6\text{Li}\{^1\text{H}\}$  and  ${}^6\text{Li}\{^{19}\text{F}\}$  CP and REDOR experiments providing clear evidence for the assignments of the peaks in the  ${}^6\text{Li}$  spectrum, these experiments can be used to measure H-Li and F-Li internuclear distances. When the  $I$  and  $S$  nuclei are present as a (relatively) isolated spin pair system, both the CP and REDOR experiments exhibit oscillations of the observed signal intensity when plotted as a function of contact time or dephasing time. These oscillations are related to the magnitude of the  $I$ - $S$  dipolar coupling which in turn de-

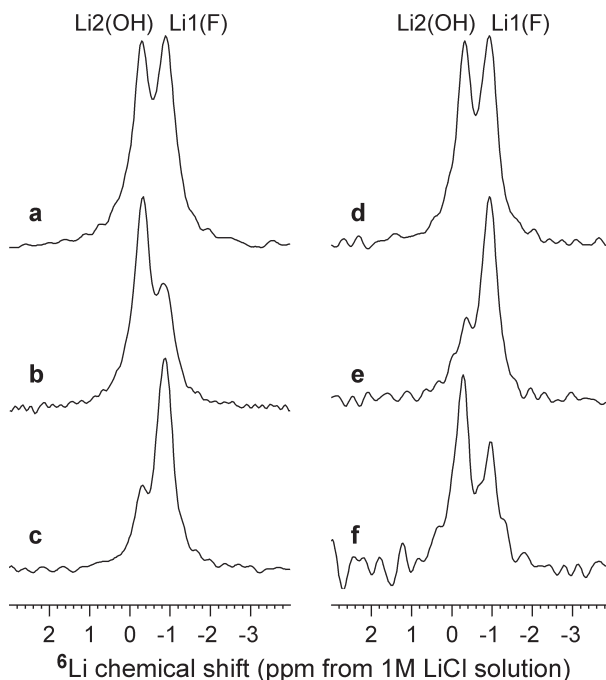


**FIGURE 12.**  ${}^6\text{Li}$  MAS NMR spectra of sample A-1. (a)  ${}^6\text{Li}$  MAS spectrum, (b)  ${}^6\text{Li}\{^1\text{H}\}$  CP MAS spectrum, (c)  ${}^6\text{Li}\{^{19}\text{F}\}$  CP MAS spectrum, (d-f)  ${}^6\text{Li}$  REDOR spectra (for rotor periods): (d) full echo, no dephasing pulses, (e)  ${}^1\text{H}$  dephasing pulses, (f)  ${}^{19}\text{F}$  dephasing pulses. The spin rate was 3.2 kHz.

pends on the  $I$ - $S$  internuclear distance.

The  ${}^1\text{H}/{}^6\text{Li}$  and  ${}^{19}\text{F}/{}^6\text{Li}$  spin pairs are relatively isolated in the amblygonite-montebbrasite samples due to several reasons: (1) the low natural abundance of  ${}^6\text{Li}$  means that the  ${}^6\text{Li}$  nuclei are well separated from each other; (2) the closest Li-F and Li-H distances, which are measured in the NMR experiments, are about 1.9 and 2.2 Å, while the next-closest Li-F and Li-H distances are 3.4–3.8 Å and 3.0–3.3 Å, respectively; (3) the presence of OH/F disorder in the sample means that only a portion of the next-nearest OH/F sites will have the same nucleus present as that being probed in the NMR experiment. The degree of isolation for  ${}^{19}\text{F}/{}^6\text{Li}$  spin pairs will be greatest in the samples at the montebbrasite end of the series with low  $F/(F + \text{OH})$  while the degree of isolation for  ${}^1\text{H}/{}^6\text{Li}$  spin pairs will be greatest in samples at the amblygonite end of the series with high  $F/(F + \text{OH})$ .

In Figure 13a the signal intensities of Li1(F) and Li2(OH) in the  ${}^6\text{Li}\{^1\text{H}\}$  CP spectra of sample A-1 are plotted as a function of the contact time (the amount of time for which magnetization is transferred from  $I$  to  $S$ ). In addition to the Li2(OH) signal being enhanced, there exists an oscillation in the signal intensity that reflects the existence of a relatively isolated two-spin system. The oscillations in this CP curve were fit using the equations introduced by Hediger (1997) and described by Fyfe et al. (2001) for a two spin-1/2 system (these equations have addition terms for damping the oscillations and for transfer of magnetization from background spins, but these are of secondary concern because it is the frequency of the oscilla-

tion that gives the dipolar coupling and internuclear distance). Because we have a (spin-1)-(spin-1/2) system, the dipolar coupling is scaled by a factor of  $\sqrt{2}$  with respect to the (spin-1/2)-(spin-1/2) system. The fit to the CP curve yielded a  $^1\text{H}$ - $^6\text{Li}$  dipolar coupling of  $1800 \pm 100$  Hz, which gives a H-Li distance of  $2.14 \pm 0.04$  Å by the relation  $D = (\mu_0 \gamma_i \gamma_s h) / (16\pi^3 r^3)$ . Similarly, the fit to the oscillations in the  $^6\text{Li}\{^{19}\text{F}\}$  CP curve (Fig. 13b) yields a dipolar coupling of  $2520 \pm 100$  Hz and a F-Li distance of  $1.88 \pm 0.03$  Å.

Figure 14 presents the  $^6\text{Li}\{^1\text{H}\}$  and  $^6\text{Li}\{^{19}\text{F}\}$  REDOR curves for sample A-1 and the calculated REDOR curves for Li2(OH) and Li1(F) respectively. The  $^1\text{H}$ - $^6\text{Li}$  dipolar coupling is determined to be  $1550 \pm 150$  Hz, which gives a H-Li distance of  $2.25 \pm 0.07$  Å. The  $^{19}\text{F}$ - $^6\text{Li}$  dipolar coupling is determined to be  $2080 \pm 80$  Hz, giving a F-Li distance of  $2.00 \pm 0.03$  Å. It is interesting to note that there is no scaling of the dipolar coupling under REDOR as there was under CP. Schmidt et al. (1992) and Quist et al. (1997) have shown that the REDOR behavior of a (spin-1)-(spin-1/2) system is equivalent to that of a (spin-1/2)-(spin-1/2) system if the spin-1 nucleus is observed and the dephasing pulses are on the spin-1/2 nucleus, but is different if the spin-1/2 nucleus is observed and the dephasing pulses are on the spin-1 nucleus (e.g.,  $^{13}\text{C}\{^2\text{H}\}$  or  $^{13}\text{C}\{^6\text{Li}\}$  REDOR experiments).

These CP and REDOR experiments were also performed for some of the other samples across the amblygonite-montebbrasite series (data not shown). The distances measured by solid-state NMR are compared to those measured by neutron diffraction in Table 12. Although the distances are in good agreement, the distances determined by CP tend to be shorter and the distances from REDOR tend to be longer. This trend is consistent with previous work on  $^{19}\text{F}/^{29}\text{Si}$  CP and REDOR experiments in octadecasil (Fyfe et al. 1997, 1999).

The CP and REDOR data reveal additional information about the nature of the disorder of the Li1 (F) and Li2(OH) sites that is not accessible by diffraction techniques. Because diffraction experiments give the average structure over the entire crystal, it is not possible to distinguish the nature of the disorder in terms of it being over domains or random throughout the crystal. The CP and REDOR data demonstrate that dipolar interactions between the two different types of sites exist through space. For example, in the  $^6\text{Li}\{^1\text{H}\}$  CP experiment, the Li1(F)

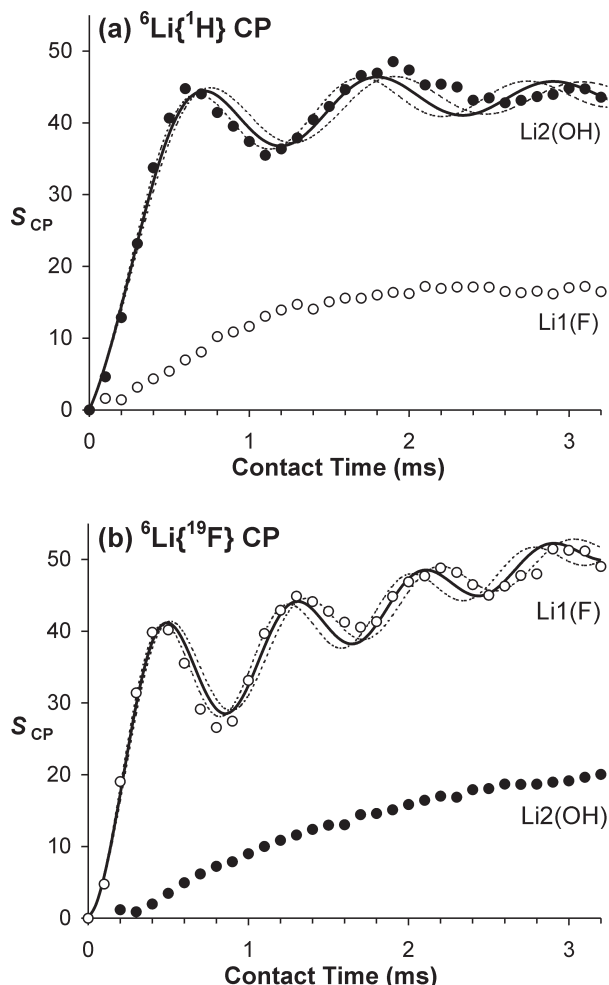


**FIGURE 13.** (a)  $^6\text{Li}\{^1\text{H}\}$  CP curves and (b)  $^6\text{Li}\{^{19}\text{F}\}$  CP curves for sample A-1. Each point represents the deconvoluted peak area from a spectrum collected with a particular contact time. The solid lines represent the calculated CP curves that best fit the data and the dashed lines represent estimates of the error. These fits yield  $^1\text{H}$ - $^6\text{Li}$  and  $^{19}\text{F}$ - $^6\text{Li}$  dipolar couplings of  $1800 \pm 100$  Hz and  $2520 \pm 100$  Hz, respectively, which give H-Li2 and F-Li1 internuclear distances of  $2.14 \pm 0.04$  Å and  $1.88 \pm 0.03$  Å.

**TABLE 12.** Summary and comparison of H-Li and F-Li distances and dipolar couplings determined by neutron diffraction, CP MAS NMR, and REDOR NMR experiments

	H-Li2 Distance (Å)			F-Li1 Distance (Å)		
	ND*	$^1\text{H}$ - $^6\text{Li}$ Dipolar Coupling (Hz)	REDOR	ND*	$^{19}\text{F}$ - $^6\text{Li}$ Dipolar Coupling (Hz)	REDOR
Dunton	$2.236 \pm 0.006$ $1581 \pm 13$	$2.14 \pm 0.04$ $1800 \pm 100$	$2.28 \pm 0.05$ $1500 \pm 100$	$1.92 \pm 0.02$ $2350 \pm 130$	—	—
AF-43	—	$2.15 \pm 0.03$ $1770 \pm 100$	$2.28 \pm 0.05$ $1500 \pm 100$	—	$1.84 \pm 0.03$ $2650 \pm 100$	$2.00(3)$ $2080(80)$
Tanco	$2.195 \pm 0.005$ $1672 \pm 12$	—	—	$1.915 \pm 0.006$ $2370 \pm 22$	—	—
A-1	—	$2.14 \pm 0.04$ $1800 \pm 100$	$2.25 \pm 0.07$ $1550 \pm 150$	—	$1.88 \pm 0.03$ $2520 \pm 100$	$2.00 \pm 0.03$ $2080 \pm 80$
AF-46	$2.191 \pm 0.005$ $1681 \pm 12$	—	—	$1.901 \pm 0.006$ $2422 \pm 23$	—	—
Saxony	$2.169 \pm 0.005$ $1732 \pm 12$	$2.15 \pm 0.03$ $1770 \pm 100$	$2.28 \pm 0.05$ $1500 \pm 100$	$1.903 \pm 0.006$ $2415 \pm 20$	$1.86 \pm 0.03$ $2580 \pm 100$	$1.98 \pm 0.05$ $2150 \pm 150$

\* Distances from neutron diffraction structures at 295 K (except Saxony, 20 K).

site still receives a significant amount of magnetization that can only come from protons in the Li2(OH) sites that are in close spacial proximity. Likewise, the  ${}^6\text{Li}\{^{19}\text{F}\}$  REDOR experiment shows dephasing of the Li2(OH) site. Again, this can only arise from the presence of  $^{19}\text{F}$  nuclei in Li1(F) sites that are close in space. These results rule out the possibility of their being large domains of one type of Li site and suggest that the disorder is random through the crystal.

Furthermore, high temperature  ${}^6\text{Li}$  MAS NMR spectra (up to 400 K) show little change (Fig. 15), indicating that there are no exchange processes involving the Li, OH, or F ions over this temperature range. This finding confirms that the disorder

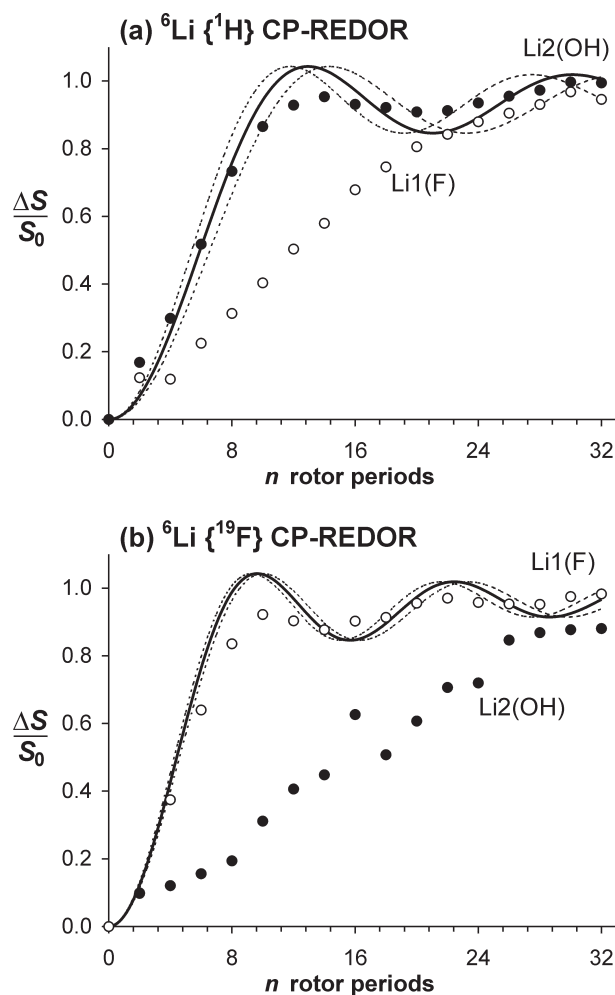


**FIGURE 14.** (a)  ${}^6\text{Li}\{^1\text{H}\}$  CP-REDOR curves and (b)  ${}^6\text{Li}\{^{19}\text{F}\}$  CP-REDOR curves for sample A-1. Each point represents the normalized difference signal,  $(S_r - S_d)/S_0$ , where  $S_0$  and  $S_d$  represent the deconvoluted peak area from the reference and dephased spectrum collected for particular dephasing time as determined by the number of rotor cycles  $n$ . The solid lines represent the calculated REDOR curves that best fit the data and the dashed lines represent estimates of the error. These fits yield  ${}^1\text{H}$ - ${}^6\text{Li}$  and  ${}^{19}\text{F}$ - ${}^6\text{Li}$  dipolar couplings of  $1550 \pm 150$  Hz and  $2080 \pm 80$  Hz respectively, which give H-Li2 and F-Li1 internuclear distances of  $2.25 \pm 0.07\text{\AA}$  and  $2.00 \pm 0.03\text{\AA}$ .

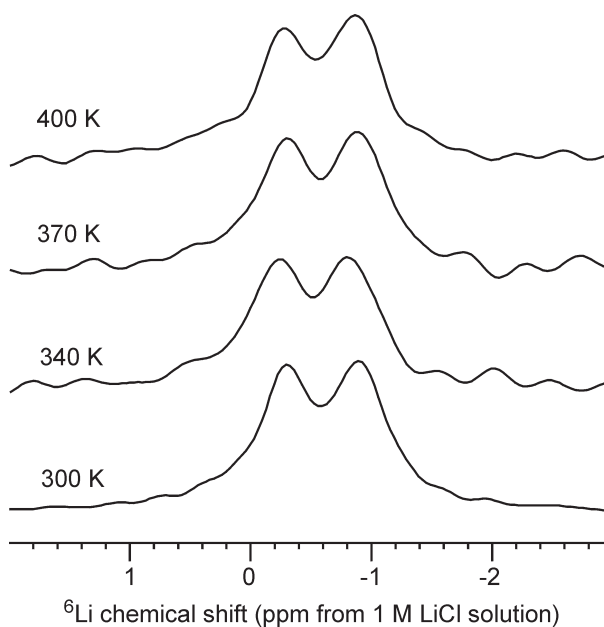


**FIGURE 15.** High-temperature  ${}^6\text{Li}$  MAS NMR spectra of sample A-1 collected at 9.4 T.

of the Li1(F)/Li2(OH) sites detected by the diffraction measurements is of a static rather than dynamic nature, and that any given Li ion has access to only one of the two sites whose precise location is determined entirely by whether OH or F is in its immediate environment. The two sites are always remote from each other on a local basis, and it is only the effect of averaging over the disordered lattice that places them in apparent close proximity in the resulting average structure.

#### ACKNOWLEDGMENTS

The authors thank P. Černý for providing sample M6116, G.R. Rossman for providing the Saxony sample, and K. Parker for typing and proofing the manuscript. The manuscript was improved by the constructive comments of J.F. Stebbins, R.L. Flemming, and R.F. Dymek. Oak Ridge National Laboratory is managed by U.T.-Battelle, L.L.C., for the U.S. Department of Energy (DoE) under contract DE-AC05-00OR22725. Argonne National Laboratory is supported by the DoE, Basic Energy Sciences under contract W-31-109-ENG-38 with the University of Chicago. Part of this research was performed in the Environmental Molecular Sciences Laboratory (a national scientific user facility sponsored by the DoE Office of Biological and Environmental Research) located at the Pacific Northwest National Laboratory, operated by Battelle for the DoE. We would like to thank the staff of the EMSL for their kind assistance and for access to their facility. Financial support was provided by the Natural Sciences and Engineering Research Council of Canada (Research Grants to L.A.G. and C.A.F.).

#### REFERENCES CITED

- Baur, W.H. (1959a) Über Kristallstrukturelle Beziehungen zwischen Amblygonit, Kierserit und Titanit. *Beiträge zur Mineralogie und Petrologie*, 6, 399–404.  
 ——— (1959b) Die Kristallstruktur des Edelamblygonits  $\text{LiAlPO}_4(\text{OH},\text{F})$ . *Acta Crystallographica*, 12, 988–994.  
 Calder, N.S., Cochran, W., Griffiths, D., and Lowde, R.D. (1962) An X-ray and neutron diffraction analysis of lithium hydride. *Journal of Physics and Chemistry of Solids*, 23, 621–632.  
 Černá, I., Černý, P., and Ferguson, R.B. (1973) The fluorine content and some physical properties of the amblygonite-montebbrasite minerals. *American Mineralogist*, 58, 291–301.  
 Dubois, J., Marchand, J., Bourguignon, P. (1972) Données mineralogiques sur la serie amblygonite-montebbrasite. *Annales de la Société Géologique de Belgique*, 95, 285–310.

- Fransolet, A.-M. and Tarte, P. (1977) Infrared spectra of analyzed samples of amblygonite-montebbrasite series: a new rapid semi-quantitative determination of fluorine. *American Mineralogist*, 62, 559–564.
- Fyfe, C.A., Lewis, A.R., Chézeau, J.M., and Grondy, H. (1997)  $^{19}\text{F}/^{29}\text{Si}$  distance determinations in fluoride-containing octadecasil from solid-state NMR measurements. *Journal of the American Chemical Society*, 119, 12210–12222.
- Fyfe, C.A., Lewis, A.R., and Chézeau, J.M. (1999) A comparison of NMR distance determinations in the solid state by cross polarization, REDOR, and TEDOR techniques. *Canadian Journal of Chemistry*, 77, 1984–1993.
- Fyfe, C.A., Brouwer, D.H., Lewis, A.R., and Chézeau, J.M. (2001) Location of the fluoride ion in tetrapropylammonium fluoride silicalite-1 determined by  $^1\text{H}/^{19}\text{F}/^{29}\text{Si}$  triple resonance CP, REDOR, and TEDOR NMR experiments. *Journal of the American Chemical Society*, 123, 6882–6891.
- Fyfe, C.A., Brouwer, D.H., Lewis, A.R., Villaescusa, L.A., and Morris, R.E. (2002) Combined solid state NMR and X-ray diffraction investigation of the local structure of the five-coordinate silicon in fluoride-containing as-synthesized STF zeolite. *Journal of the American Chemical Society*, 124, 7770–7778.
- Greiner, D.J. and Bloss, F.D. (1987) Amblygonite-montebbrasite optics: response to  $(\text{OH}^-)$  orientation and rapid estimation of F from 2V. *American Mineralogist*, 72, 617–624.
- Groat, L.A., Raudsepp, M., Hawthorne, F.C., Ercit, T.S., Sherriff, B.L., and Hartman, J.S. (1990) The amblygonite-montebbrasite series: Characterization by single-crystal structure refinement, infrared spectroscopy, and multinuclear MAS-NMR spectroscopy. *American Mineralogist*, 75, 992–1008.
- Gullion, T. and Schaefer, J. (1989a) Rotational-echo double resonance NMR. *Journal of Magnetic Resonance*, 81, 196–200.
- (1989b) Detection of weak heteronuclear dipolar coupling by rotational-echo double-resonance nuclear magnetic resonance. *Advances in Magnetic Resonance*, 13, 57–83.
- Harris, R.K. and Minoja, A.P. (1995) Use of cross-polarization in lithium-6 solid state NMR. *Magnetic Resonance in Chemistry*, 33, 152–155.
- Hawthorne, F.C., Groat, L.A., Raudsepp, M., and Ercit, T.S. (1987) Kieserite,  $\text{Mg}(\text{SO}_4)(\text{H}_2\text{O})$ , a titanite-group mineral. *Neues Jahrbuch für Mineralogie Abhandlungen*, 157, 121–132.
- Hediger, S. (1997) Improvement of heteronuclear polarization transfer in solid-state NMR, 179 p., Ph.D. Thesis, Eidgenössische Technische Hochschule, Zürich.
- Kallio, P. (1978) A new X-ray method for the estimation of fluorine content in montebbrasites. *American Mineralogist*, 63, 1249–1251.
- London, D., Morgan, G. B. VI, and Wolf, M.B. (2001) Amblygonite-montebbrasite solid solutions as monitors of fluorine in evolved granitic and pegmatitic melts. *American Mineralogist*, 86, 225–233.
- Moss, A.A., Fejer, E.E., and Embrey, P.G. (1969) On the X-ray identification of amblygonite and montebbrasite. *Mineralogical Magazine*, 37, 414–422.
- Penner, G.H. and Hutzal, J. (1997) A lithium-6 CP/MAS standard. *Magnetic Resonance in Chemistry*, 35, 222–226.
- Quist, P.-O., Förster, H., and Johnels, D. (1997) A  $^6\text{Li}-^{13}\text{C}$  REDOR study of the TMEDA complex of solid fluorenyllithium. *Journal of the American Chemical Society*, 119, 5390–5397.
- Satyanarayan, M.N., Deepthy, A., and Bhat, H.L. (1999) Potassium titanyl phosphate and its isomorphs: Growth, properties, and applications. *Critical Reviews in Solid State and Materials Sciences*, 24, 103–191.
- Schmidt, A., McKay, R.A., and Schaeffer, J. (1992) Internuclear distance measurement between deuterium ( $I = 1$ ) and a spin-1/2 nucleus in rotating solids. *Journal of Magnetic Resonance*, 96, 644–650.
- Simonov, W.I. and Belov, N.W. (1958) Die Aufklärung der Struktur des Amblygonits mit Hilfe der Minimum Funktion. *Kristallografia*, 3, 428–437.
- Vidal, J.P. and Vidal-Valat, G. (1986) Accurate Debye-Waller factors of  $^7\text{LiH}$  and  $^7\text{LiD}$  by neutron diffraction. *Acta Crystallographica*, B42, 131–137.
- Von Dreele, R.B., and Larson, A.C. (1998) GSAS, General Structure Analysis System, Los Alamos National Laboratory Report LAUR 86-748, 185 p.
- Wolfram, S. (1996) Mathematica: A System for Doing Mathematics by Computer. Wolfram Media, Champaign, Illinois.
- Xu, Z. and Stebbins, J.F. (1995)  $^6\text{Li}$  nuclear magnetic resonance chemical shifts, coordination number relaxation in crystalline and glassy silicates. *Solid State Nuclear Magnetic Resonance*, 5, 103–112.

MANUSCRIPT RECEIVED FEBRUARY 12, 2002

MANUSCRIPT ACCEPTED SEPTEMBER 2, 2002

MANUSCRIPT HANDLED BY ROBERT F. DYMEK